

ABSTRACT

RESULTS OF BEAM TESTS OF A PROTOTYPE CALORIMETER FOR A LINEAR COLLIDER

Kurt Francis, Ph.D.
Department of Physics
Northern Illinois University, 2010
Gerald C. Blazey, Director

The proposed International Linear Collider (ILC) requires a detector with superior jet energy resolution of $30\%/\sqrt{E}$ or better near the Z-pole region (91GeV). The Calorimeter for the Linear Collider Collaboration (CALICE) is developing and testing prototype detectors with this goal in mind. One major limitation on detector resolution is the size of the hadron calorimeter contained within a magnetic coil. To compensate for “thin” calorimeters that cannot contain the highest energy particle showers, the Tail Catcher/Muon Tracker (TCMT) has been designed to include calorimetric functions and higher granularity than existing muon tracking systems. The prototype design also provided an opportunity to simulate the impact of a magnetic coil on energy resolution and to study the use of silicon photomultipliers (SiPMs) in particle detectors.

This analysis shows that a TCMT six interaction lengths deep contains leakage and improves energy resolution when added to the CALICE electromagnetic and hadronic calorimeters. The effect of the TCMT both with and without a coil is more significant as energy increases. The addition of all sixteen layers of the TCMT to a 3.5 interaction length thick calorimeter improves pion resolution by 9.3% at 20 GeV and 10.8% at 80 GeV. For a 5.5 interaction length thick calorimeter system, typical of those

under consideration for ILC detectors, the addition of TCMT layers after a coil of 1.8 interaction lengths improves energy resolution of 20 GeV pions by 1% and for 80 GeV pions by 2%.

NORTHERN ILLINOIS UNIVERSITY
DE KALB, ILLINOIS

MAY 2010

RESULTS OF BEAM TESTS OF A PROTOTYPE CALORIMETER FOR A LINEAR
COLLIDER

BY

KURT FRANCIS
©2010 Kurt Francis

A DISSERTATION SUBMITTED TO THE GRADUATE SCHOOL
IN PARTIAL FULFILLMENT OF THE REQUIREMENTS
FOR THE DEGREE
DOCTOR OF PHILOSOPHY

DEPARTMENT OF PHYSICS

Dissertation Director:

Gerald C. Blazey

ACKNOWLEDGEMENTS

I would like to thank Vishnu Zutshi for his leadership and direction in the project, Guilherme Lima for establishing the analysis framework and training me in its use, and Gerald Blazey, my thesis advisor, for his ongoing advice and direction and patience. I would also like to thank all the other members of the Northern Illinois Center for Accelerator and Detector Development and the CALICE collaboration without whose efforts there would be no detectors, test beam experience or data for analysis.

DEDICATION

For Melissa, Emma and Kira

TABLE OF CONTENTS

	Page
LIST OF TABLES	vi
LIST OF FIGURES	vii
 Chapter	
1 INTRODUCTION	1
2 CALORIMETRY	10
3 THE TAILCATCHER / MUON TRACKER	18
3.1 Introduction	18
3.2 Design Motivations	19
3.3 Mechanical Structure/Absorber	20
3.4 Active Layers	21
3.5 TCMT with CALICE Calorimeters at the CERN Test Beam	27
4 CALICE INSTALLATION AT THE CERN TEST BEAM	33
5 CALIBRATION AND STABILITY	40
5.1 Introduction	40
5.2 SiPM Gain Determination	40
5.3 MIP Calibration	44
5.4 Light Yield Determination	46
5.5 Pedestal Stability	48

Chapter	Page
5.6 Temperature Effects and Preliminary Sampling Weights	50
6 TOWARDS A CLEAN SAMPLE.....	53
6.1 Introduction.....	53
6.2 Signal Threshold Cut	53
6.3 Cuts Based on In-Beam Counters	54
6.4 Energy to Hit Ratio Cut	58
7 DETERMINATION OF THE SAMPLING WEIGHTS	64
8 DETERMINATION OF THE SiPM SATURATION CORRECTION	71
9 RESOLUTION AND LINEARITY AS A FUNCTION OF CALORIMETER THICKNESS	85
9.1 Resolution as a Function of Calorimeter Thickness	85
9.2 Separation of Stochastic and Constant Components of Resolution.....	87
9.3 Linearity.....	89
9.4 Leakage	90
10 COIL STUDIES.....	92
11 CONCLUSIONS.....	100
REFERENCES	102

LIST OF TABLES

Table	Page
3.1 TCMT Layers Used for Analysis.....	32
4.1 Calibrated Run List for Pions	35
6.1 Cherenkov Electron Efficiency.....	55
6.2 Ratio Cut Efficiency	61
6.3 Breakdown of Event Types.....	63
7.1 Intercalibration Weights with Layers of the TCMT Added to the Calorimeter System Derived from a 20 GeV Negative Pion Sample	69
7.2 Intercalibration Weights with Layers of the TCMT Added to the Calorimeter System and Used to Simulate a Magnetic Coil and for Post-coil Sampling from a 20 GeV Negative Pion Sample	70
8.1 Response of a Sample SiPM	75
8.2 Alternative Methods of Calculating Interpolated Scaling Factors.....	77
9.1 Leakage Measurements.....	91
10.1 TCMT Layers Used for Coil Simulation Analysis	93

LIST OF FIGURES

Figure	Page
1.1 Particles of the standard model	3
1.2 International Linear Collider (ILC) diagram	6
1.3 Comparison of LHC and ILC events in simulated detectors	6
2.1 Relative improvement in separation of Z and W di-jet masses for jet resolution of 60% and 30%	17
3.1 CALICE detectors at CERN test beam 2006.....	19
3.2 TCMT absorber structure showing fine and coarse sections	20
3.3 Extruded scintillator segments.....	22
3.4 TCMT cassette frame.....	25
3.5 SiPM on holder	25
3.6 TCMT fully instrumented at CERN test beam 2007	29
3.7 Diagram of CALICE detector in October 2006 showing main sections	29
3.8 Diagram of CALICE HCAL during October 2006 CERN run period showing the order of absorber and active layers.....	30
3.9 Diagram of CALICE TCMT showing the order of active layers and absorber layers of two different thicknesses	30
3.10 Diagram of TCMT for example Configuration 3	32
4.1 Diagram of CERN accelerator complex	34
4.2 Block diagram of CALICE detectors at CERN 2006 test beam with an example schematic hadron shower in the HCAL extending into TCMT ...	34

Figure	Page
4.3 Example response of the Cherenkov detector as a function of pressure in an 80 GeV pion beam	37
4.4 Detailed spacing diagram of CALICE detectors	38
5.1 Typical photoelectron spectrum.....	42
5.2 Distribution of gains	43
5.3 Example of MIP spectrum with Gaussian fit.....	45
5.4 MIP calibration values	46
5.5 Calculated light yield for 135 TCMT strips.....	47
5.6 Effective light yield for working strips	48
5.7 Percent change in pedestals of one layer between four different runs.....	49
5.8 RMS change in pedestals for each layer between four runs	49
5.9 Correlation plot used to determine the intercalibration constant with a hand-drawn line estimating the correlation.....	52
6.1 Energy spectrum for ECAL+HCAL+TCMT detector with no cuts	54
6.2 Energy spectrum for ECAL+HCAL+TCMT detector with Cherenkov detector cut to remove electrons	55
6.3 Veto counter amplitude.....	56
6.4 Energy spectrum for total detector with electron and multi-particle cuts applied.....	57
6.5 Energy spectrum of total detector with muon veto, electron and multi-particle cuts applied.....	58
6.6 Energy to hit ratios from a muon run in ECAL, HCAL and TCMT	60
6.7 Energy spectrum with energy to hit ratio, muon veto, electron and multi-particle cuts applied.....	62

Figure	Page
8.1 Diagram of silicon photomultiplier (SiPM) structure.....	72
8.2 Photo of SiPM.....	73
8.3 Detail of SiPM pixel structure	73
8.4 Measured response of a typical SiPM and expected response if the device were linear	74
8.5 Plot of energy resolution to compare Method 3 and Method 4 for the calculation of interpolation scaling factors	78
8.6 Plot of linearity to compare Method 3 and Method 4 for the calculation of interpolation scaling factors.....	79
8.7 Hit energy spectrum for a 20 GeV pion run	80
8.8 Corrected versus uncorrected event energy	80
8.9 Average response of all strips for a 20 GeV pion run.....	81
8.10 Maximum response of all strips for a 20 GeV pion run	81
8.11 Increase in energy in MIPS due to saturation correction algorithm for individual hits.....	82
8.12 Increase in energy in MIPS due to saturation correction algorithm for event totals	83
8.13 Ratio of saturation corrected to uncorrected event total energies in TCMT..	83
8.14 Ratio of event energy with and without saturation correction as a function of beam energy	84
9.1 Comparison of the energy spectrum with and without full TCMT	86
9.2 Energy resolution as a function of interaction lengths used in the TCMT ...	88
9.3 Energy resolution of the full calorimeter response to negative pions as a function of energy with a second-degree polynomial.....	89
9.4 Linearity	90

Figure		Page
10.1	Energy spectra with zero layers of TCMT added to the calorimeter system and with simulated coil and subsequent post-coil sampling for an 80 GeV pion run.....	94
10.2	Comparison of the energy resolution of a 20 GeV negative pion sample with a simulated coil with and without final TCMT layers after coil.....	95
10.3	Resolution as a function of inner calorimeter depth inside the simulated coil and with subsequent sampling	96
10.4	Resolution as a function of beam energy for four different coil depths with subsequent sampling	97
10.5	Energy resolution versus energy for a 5.5λ calorimeter system without a coil and followed by a simulated coil and post coil sampling	98
10.6	Relative change in resolution with and without coil and subsequent sampling.....	99

CHAPTER 1

INTRODUCTION

High-energy physics involves the basic building blocks of the universe and the forces by which they interact. Our collective understanding of the particles of matter and the fundamental forces is referred to as the Standard Model (SM) of particle physics. The particles of matter are either quarks or leptons. The quarks are bound together in groups of three to form composite particles called baryons such as the protons and neutrons that make up the nuclei of atoms, or into pairs to form mesons, such as pions and kaons. Leptons, unlike quarks do not bind together. The leptons include electrons, muons, taus and the neutrinos.

Quarks and leptons occur in three families. Each family has a quark doublet with a $+2/3$ charged quark and a $-1/3$ charged quark and a lepton doublet with a -1 charged member like the electron and a neutral member called a neutrino. The property that distinguishes one quark from its doublet partner is called its flavor.

The first family has the lowest overall mass and is therefore the most stable of particles. The up (u) and down (d) quarks form the quark doublet in the first family. The proton is a composite of uud quarks and the neutron a composite of udd quarks. The electron and the electron neutrino form the lepton doublet of the first family. The other

two families are more massive and unstable and ultimately decay into members of the first family.

The second family consists of the charm (c) quark, with a $+2/3$ charge (like the u quark), the strange (s) quark, with a $-1/3$ charge (like the d quark), the muon (with a -1 electric charge like the electron) and the muon neutrino. The third family consists of the top quark (t), the bottom quark (b), the tau lepton and the tau neutrino.

For each quark and lepton there is an anti-particle with the same mass but opposite properties. Anti-particles are usually named simply by putting “anti-“ before the species name, like anti-quark, or anti-up. The anti-electron is also called a positron.

Each particle interacts with others through the exchange of force carrying particles that are associated with each of the fundamental forces. The charged particles interact via the electromagnetic force through the exchange of photons. The charges are either positive, $+$, or negative, $-$, with opposite charges being attractive and like charges being repulsive. The weak nuclear force is carried by W^+ , W^- , and Z gauge bosons. The W^+ and W^- change the flavor of the interacting particles as well as momentum.

Quarks possess an attribute called “color” that characterizes the strong force. Color is akin to electric charge except that there are three colors instead of the two kinds of electric charge: positive and negative. Where positive and negative electric charges form electrically neutral systems when paired, colored particles form color neutral composites when in groups of two or three. The term color arises from analogy with optics where three primary colors, red, green and blue, form the color neutral combination white. Anti-quarks possess a similar color triplet that when combined is also

color neutral. A quark possessing a color can also pair up with an anti-quark with its anti-color also forming a color neutral combination called a meson such as the pion or kaon. The strong force is carried by gluons which is a mixed state of color and anti-color. The strong force binds quarks into baryons or mesons. Fig 1.1 [1] graphically summarizes the particles of the standard model.

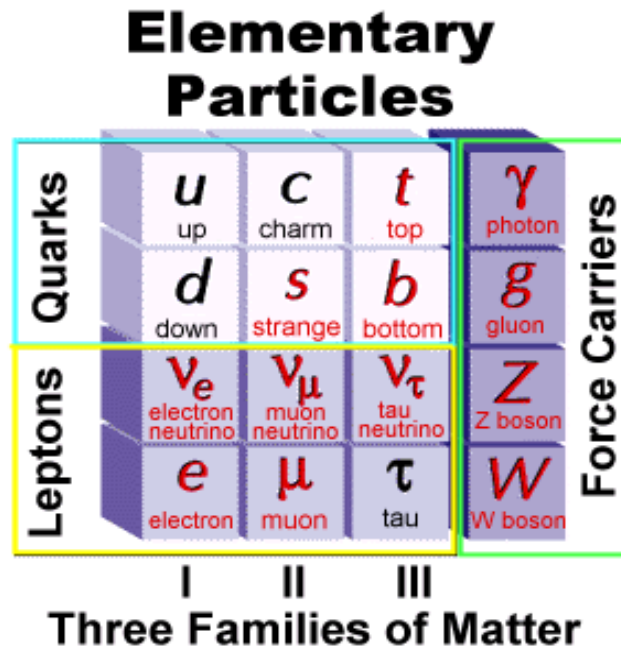


Figure 1.1: Particles of the standard model.

Two of the main goals of particle physics are to discover all the fundamental particles and to unify the fundamental forces. The electromagnetic force and weak nuclear force have been successfully unified as the electroweak interaction with the

photon, W^+ , W^- , and Z^0 bosons as the carriers of the interaction. The photon is massless and therefore gives the electromagnetic interaction infinite range. The other gauge bosons are massive and it is this mass that limits the range and causes the apparent weakness of the interaction. The acquiring of mass by the electroweak gauge bosons is referred to as spontaneous symmetry breaking and is believed to be caused by another field called the Higgs field. Interactions with the Higgs field give gauge bosons and possibly other particles the fundamental property of mass [2]. The quantum of the Higgs field is called the Higgs boson. The quest to discover the Higgs boson and study its properties has been a major driver in the design of machines and experiments in the field.

To study these subatomic particles, high-energy machines called particle accelerators are used to accelerate beams of protons or electrons and their anti-particles, common, stable particles that make up ordinary matter, to very high energies. Beams can be directed to a fixed target, to form a beam of secondary particles, like neutrinos, or for testing purposes, or are made to collide with a second beam traveling in opposite directions. Large detectors use a variety of different techniques to study the products of these collisions, some of which may be exotic new particles.

To further our understanding of the SM and the Higgs boson and to explore beyond the standard model, larger, more powerful and more precise machines are required. Currently, the Tevatron at Fermi National Accelerator Laboratory (Fermilab) in Batavia, Illinois, and the Large Hadron Collider (LHC) at the European Organization for Nuclear Research (CERN) in Geneva, Switzerland, are the most powerful accelerators in the world. The Tevatron collides protons with anti-protons. The LHC collides protons

with protons. Since both machines use protons or anti-protons, which are in turn made of quarks, the left over partons not involved in the hard collisions also register in the detectors. Partons can be quarks or gluons. The LHC also has a high collision rate which creates “noisy” events. An additional disadvantage at the LHC is that the initial state is poorly defined. The collision could be between quarks, between quarks and gluons, or between gluons.

A linear electron collider has been proposed as the next generation collider beyond the LHC. The linear collider would use electrons and anti-electrons or positrons (Fig 1.2), both, to the best of our knowledge, structureless particles [3]. Though the International Linear Collider (ILC) would operate at lower energies than the LHC it would be capable of comparable performance because the electrons and positrons are fundamental particles and all of their energy would be converted in the reaction to new states of matter. The LHC, in contrast, uses protons, which, being composite particles bestow only approximately 10% of their energy to interacting constituents. At the ILC the initial state would also be clearly defined: a collision between an electron and positron. The rate is designed to be lower and the final states do not have remnant partons. High precision physics is therefore possible. Fig 1.3 compares simulated events in an LHC detector and in an ILC detector. [4] Both events contain a Higgs boson. In the LHC example on the left, the only part of the signal due to the Higgs is the two small jets of particles (in red and pointed to by black arrows in the figure), the rest is “noise” due to other particles in the event and remnant partons. In the ILC example, two quark jets are easy to separate and measure and two other tracks are due to Z boson decays into leptons.

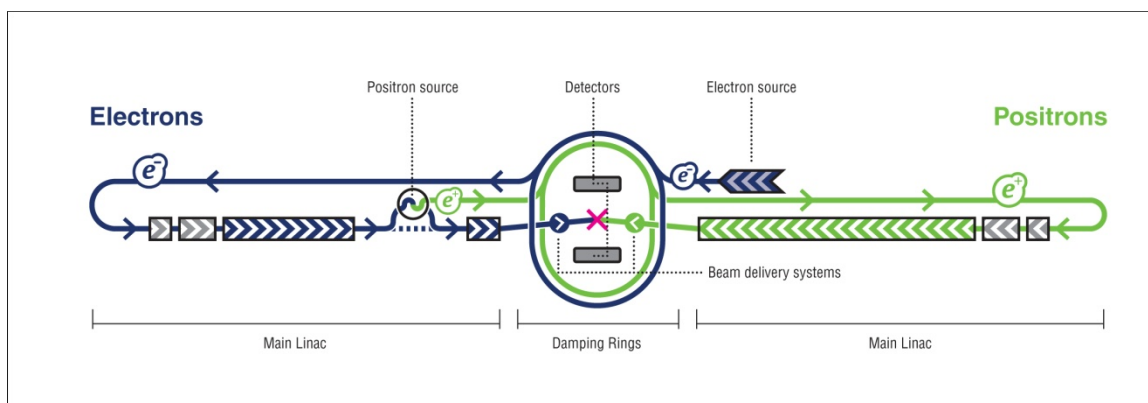


Figure 1.2: International Linear Collider (ILC) diagram.

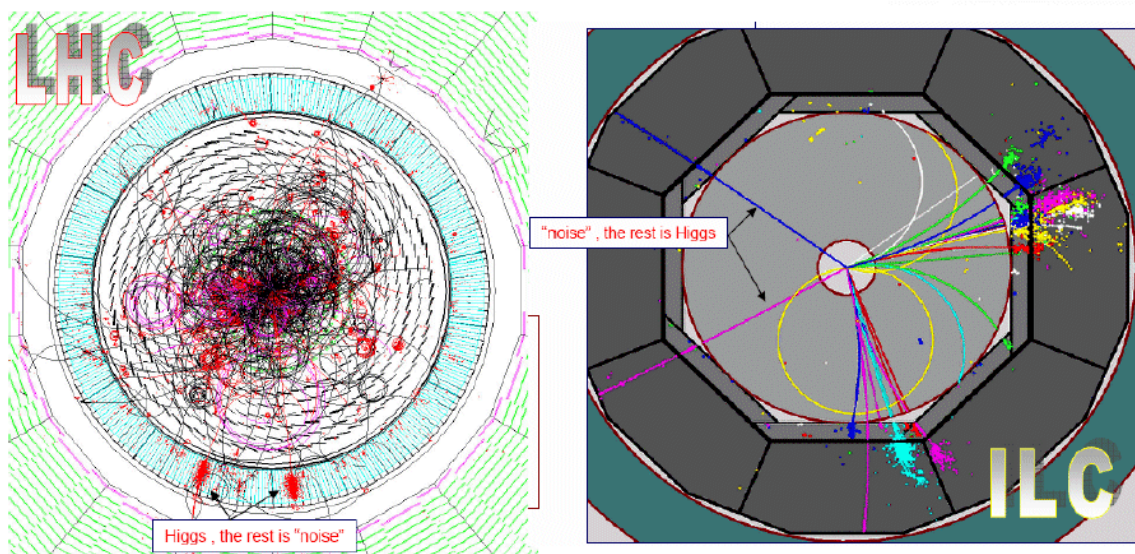


Figure 1.3: Comparison of LHC and ILC events in simulated detectors.

General purpose collider detectors have a nested design with a number of different components each with a specialized function. They typically have a cylindrical structure surrounding the interaction point. Closest to the beam pipe where the collision occurs is the tracker which measures the trajectory and momentum of charged particles. An electromagnetic coil surrounding the tracker generates a magnetic field in the tracker that bends the path of charged particles. The direction of the curve determines the sign of the particle charge and the magnitude of the curve helps determine the particle momentum. Outside of the tracker (and typically outside of the coil) are the electromagnetic and hadronic calorimeters (which measure the energy of the product particles of the particle collision) which, in turn, are surrounded by a muon tracking system at the largest distance from the interaction regions.

The designs for the ILC detectors feature calorimeters inside the coil so that momentum information can be extracted from tracks inside the calorimeter. Ideally, for optimal tracking and energy resolution, the calorimeter and coil would be as large as possible. However, cost and engineering considerations put strong practical limits on the size of the hadronic calorimeter. Practical calorimeters are thin enough such that some particle energy, the tail of the energy distribution, escapes detection. The SID calorimeter design has a combined calorimeter thickness of 5.5λ [5]. In comparison, the more traditional designs of the CDF and D0 detectors at Fermilab have calorimeters in the range of 7 to 10λ thick [6]. A way to compensate for this is to add “tail-catching” calorimetric capabilities to the standard muon tracking system, hence a tail catcher/muon tracker.

The Calorimeter for the Linear Collider (CALICE) [7] collaboration has developed a prototype detector for the ILC featuring three components, an electromagnetic calorimeter (ECAL), a hadron calorimeter (HCAL), and a Tail Catcher/Muon Tracker (TCMT) to study new technologies and techniques required to optimize the performance of detectors for the linear collider. The Northern Illinois Center for Accelerator and Detector Development (NICADD), with support from Deutsches Elektronen-Synchrotron (DESY) and Fermilab, is responsible for the prototype CALICE TCMT.

Particles entering the calorimeters interact with absorber material and generate showers of secondary particles. These secondary particles leave signals in the active layers and produce their own secondary particles in the absorber. The magnitude of the signal in all the active layers is combined and used to reconstruct the original particle's energy. As the shower penetrates deeper in the calorimeter system less energy is available to generate secondary particles and eventually the shower is largely absorbed in the detector.

Like the calorimeters, the TCMT consists of alternating layers of absorber and active layers. In the case of the TCMT the absorbers are steel and the active layers are extruded plastic scintillator with wavelength shifting fibers directing light generated by the passage of charged particles to silicon photomultipliers (SiPM). Most of the particle energy is absorbed by the ECAL and HCAL subsystems; however, a "tail" of shower particles and muons can make it into the TCMT. There they interact with strips of plastic scintillator producing photons of light. In each strip, the photons are collected by an

optical fiber that directs the light to a SiPM, a small device the size of a pencil eraser that converts that light into an electrical signal that can be digitized and fed into a computer. The SiPMs, due to their small size, low power requirements and immunity to magnetic fields, can replace much larger photomultiplier tubes that have been used in other detectors [8]. These are novel devices and prior to the CALICE effort, not tested in a large scale calorimeter prototype. The energy measured in the active TCMT layers can then be added to the energy measured in the HCAL to find the particle's total energy. Muons have a lower energy loss rate and tend to pass all the way through the calorimeters and into the TCMT. The muon tracking data is collected in the TCMT and can be combined with data from the HCAL and ECAL in the complete analysis of the event.

The first of the active TCMT layers was produced in 2005 and tested at the electron test beam at DESY in Hamburg Germany. The same layer was tested at the Meson Test Beam Facility at Fermilab in February 2006. Throughout 2006, a calibration system was developed and sixteen layers were assembled, tested and calibrated. Data was taken with the full TCMT at the CERN test beam in the summer and fall of 2006.

This dissertation discusses the design and calibration of the TCMT and analysis of test beam data to study the effects of various configurations of the TCMT on single particle energy resolution. The analysis of TCMT test beam data is necessary to help evaluate new detector designs that are needed to develop an informed proposal for the future ILC detector. New technology used in the TCMT such as the SiPMs and extruded scintillator also have applications in other branches of science and medicine.

CHAPTER 2

CALORIMETRY

Large detectors for particle colliders have a number of components optimized for specific tasks that together enable the collection of data needed to reconstruct particle interactions or “events”. A tracker placed close to the beam pipe and therefore close to the interaction point tracks the path of charged particles emerging from the interaction. The magnetic field generated by a magnetic coil bends the paths of charged particles. Tracing the direction of the curve in the track allows one to determine the charge of the particle, and the degree of curvature determines the momentum of the particle. Outside the tracker is the calorimeter.

Calorimeters, which typically include electromagnetic (ECAL) and hadronic calorimeters (HCAL), measure the total energy of the particles produced in the reaction. Nearly all of the particle energy is absorbed in the calorimeter. Incoming particles interact with matter in a variety of ways and most of these mechanisms create secondary particles which are often of high enough energy to produce tertiary particles of lower and lower energy until they reach a low energy cut off. This resultant cascade is called a “shower.”

A sampling calorimeter consists of layers of absorber material such as steel that separate active layers of detector such as scintillator. The active layer is connected to a

photo-detector such as a photo-multiplier tube or the SiPM used in the CALICE hadronic calorimeter and TCMT. As the particle passes through the absorber layers, eventually all of the particle's energy is absorbed and the particle is "stopped" in the detector. A detector that absorbs all the particles in a shower is called hermetic.

An ECAL is designed to measure and contain showers initiated by particles that interact electromagnetically such as photons and electrons. Energy loss by photons at low energy is due mostly to ionization with some Compton scattering, Rayleigh scattering, and photo nuclear absorption. At high energy it is due mostly to pair production in which the photon interacts with a nucleus to form an electron – positron pair. Energy loss by electrons at low energy is also due to ionization and at high energy by bremsstrahlung [9]. The amount of matter traversed by a particle before interacting is given in radiation lengths, X_0 , with units g/cm^2 . An ECAL is typically designed to have a thickness of about 24 radiation lengths, which fully contains the electromagnetic component of a shower.

A HCAL is designed to measure the hadronic component of a jet. Hadrons are particles which interact strongly with the nuclei of atoms in the absorber. Hadrons include baryons, like protons and neutrons, and mesons, like pions. The charged hadrons are detected in the tracker and leave energy in the ECAL as well as the HCAL but the uncharged hadrons like neutral pions, neutrons and neutral kaons are primarily detected in the HCAL. The thickness of a hadronic calorimeter can be stated in terms of nuclear interaction lengths, λ_{int} . The nuclear interaction length is the average distance a high-

energy hadron must travel inside a medium before nuclear interaction occurs [10]. A typical hadronic calorimeter is five or more interaction lengths in depth.

No calorimeter is perfectly hermetic, so some shower energy leaks out. The design of detectors requires engineering tradeoffs that attempt to achieve a balance between performance and cost. To improve performance it is desirable to place the calorimeter inside the unsampled material of the magnetic coil. However this would result in a large, expensive magnet. Alternately the tracking system and the coil could be entirely inside the calorimeter which results in poorer performance as the material in the coil absorbs some of the shower energy and increases calorimeter cost due to size. As a result there are cost and performance tradeoffs between the position and size of the coil and calorimeter.

Outside of the calorimeter and coil, a muon system tracks muons, almost all of which penetrate the calorimeter. Muons are very similar to electrons except that they are 200 times more massive. This greater mass leads to a bremsstrahlung rate that is much lower than electrons. Ionization is, therefore, the primary means for muons to lose energy if their energy is less than 50 GeV. The muon tracking data collected can be combined with data from the inner tracker and the calorimeter to complete the analysis of an event.

The Silicon Detector for the ILC (SiD) [11] design proposal suggests a calorimeter around 5.5 interaction lengths thick. Monte Carlo simulations show that this is too thin to contain many showers so further sampling beyond the coil is necessary to achieve good particle energy resolution. A logical step would be to add sampling

capabilities to the muon system which is placed outside the coil. This is one of the primary motivations for a TCMT.

Considering the CALICE prototype detector, the TCMT completes the sampling of particle showers and is also the muon tracking system. Like the HCAL, the TCMT consists of layers of steel absorber that separate active layers of extruded plastic scintillator with wavelength shifting fibers directing the detected light to SiPMs. Most of the particles are absorbed by the ECAL and HCAL subsystems. The "tail" particles and muons that make it into the TCMT interact with strips of plastic scintillator producing a small amount of light. The energy measured in the TCMT layers can then be added to the energy measured in the ECAL and HCAL to estimate the total particle energy.

An important figure of merit of a detector is energy resolution, E_{res} , the relative precision of the energy measurement:

$$E_{\text{res}} = \sigma/E_{\text{total}}$$

where E_{total} is the mean response of the calorimeter and σ , the standard deviation of the response. The resolution is due to a combination of several effects which can be parameterized in the following way:

$$\frac{\sigma(E)}{E} = \sqrt{\frac{N^2}{E^2} + \frac{S^2}{E} + C^2} = \frac{N}{E} \oplus \frac{S}{\sqrt{E}} \oplus C$$

where N is a "noise" term due mostly to electronics, S is a "stochastic" term due to statistics-related shower fluctuations, photoelectron (PE) statistics, dead material in front of the calorimeter, and sampling fluctuations [12], and C is a "constant" term due to

detector non-uniformity, calibration uncertainty and leakage. The stochastic and noise terms are uncorrelated [13].

Partons (quarks or gluons) emanating from an interaction typically manifest themselves as “jets” of particles primarily composed of mesons and other hadrons. The energy of the jet is assigned to the parton. Jet energy resolution is approximated as:

$$\frac{\sigma(E)}{E} \approx \alpha / \sqrt{E_{jj}(\text{GeV})}$$

where E_{jj} is the energy of the dijet system. This is also equivalent to the dijet mass resolution:

$$\frac{\sigma(M)}{M} \approx \frac{\alpha}{\sqrt{E_{jj}}}$$

An expected Higgs production channel at the ILC would be $e^-e^+ \rightarrow Z^* \rightarrow ZH$. The Z (as well as the H) can decay into a lepton / anti-lepton pair or a quark / anti-quark pair. The quark / anti-quark pair is detected as jets. W and Z bosons created by other processes can also decay into jets ($Z \rightarrow q\bar{q} \rightarrow 2 \text{ jets}$ and $W \rightarrow q\bar{q} \rightarrow 2 \text{ jets}$). Since W and Z bosons are similar in mass the ILC detector must have sufficient jet energy resolution to readily distinguish between W and Z decays. This can be done if $\sigma(M) \approx \Gamma_{W/Z} \approx 2 \text{ GeV}$, the natural decay width for the Z and W decays. For the W boson decay with a mass of $\sim 80 \text{ GeV}$ the required dijet mass resolution is approximately 0.027. For a jet in the 100 GeV range:

$$\frac{\sigma(M)}{M} \approx \frac{2\text{GeV}}{80\text{GeV}} \approx 0.027 = \frac{\alpha}{\sqrt{E_{jj}}} = \frac{\alpha}{\sqrt{100\text{ GeV}}}$$

This leads to an $\alpha = 0.027\sqrt{100} = 0.27$. For a 200 GeV jet $\alpha = 0.38$. A reasonable target is:

$$\frac{\sigma(E)}{E} \approx 30\%/\sqrt{E(\text{GeV})}.$$

This resolution goal is a factor of two better than existing calorimeters which have a value of α between 60% and 80%. Fig. 2.1 [14] shows the relative improvement in separation of Z and W particle di-jet masses for 60% and 30% resolution. At 30%, the case with superior resolution, it is easier to separate Z and W particle decays which have energies of 91 GeV and 80 GeV respectively.

In an attempt to improve calorimeter resolution, Particle Flow Algorithms (PFA) have been proposed. In a jet, approximately 60% of the energy is in charged hadrons, 30% in photons and 10% in neutral hadrons. In the past, all the jet energy was measured simply with calorimetry with approximately 70% of the energy measured in the HCAL which has the poorest resolution. With PFA algorithms the entire detector is used to measure jet energy by reconstructing all visible particles in the event with each component (tracker, ECAL, and HCAL) used to measure what it can measure best.

The tracker, with traditionally excellent momentum resolution, is used to measure the energy of charged particles. The ECAL is used to measure the energy of photons. The HCAL is used for measuring the energy of only neutral hadrons. To implement PFA the

showers in the HCAL from charged particles have to be identified and subtracted from the total leaving only the showers from neutrals measured in the HCAL. High granularity is required to give the HCAL the ability to identify individual particle tracks.

Confusion on hits assignment stems from three main sources. The first is the failure to resolve photons in the ECAL if the photon shower can not be separated from an additional track. The second comes from the failure to resolve neutral hadrons because those hits are incorrectly assigned to the shower of a charged hadron. The third comes from the incorrect assignment of hits in the fragment of a shower of a charged hadron to a neutral hadron. High granularity in both the ECAL and HCAL is necessary to help reduce these effects. A TCMT will also permit full sampling of the neutral hadrons.

PFA requires extensive offline analysis and the algorithms are in development. The offline algorithm must be integrated into the detector design. Pandora PFA, currently one of the most advanced algorithms, can achieve $\sigma_E/E \leq 3.8\%$ for jets of 40 – 400 GeV [15] meeting the 30% goal.

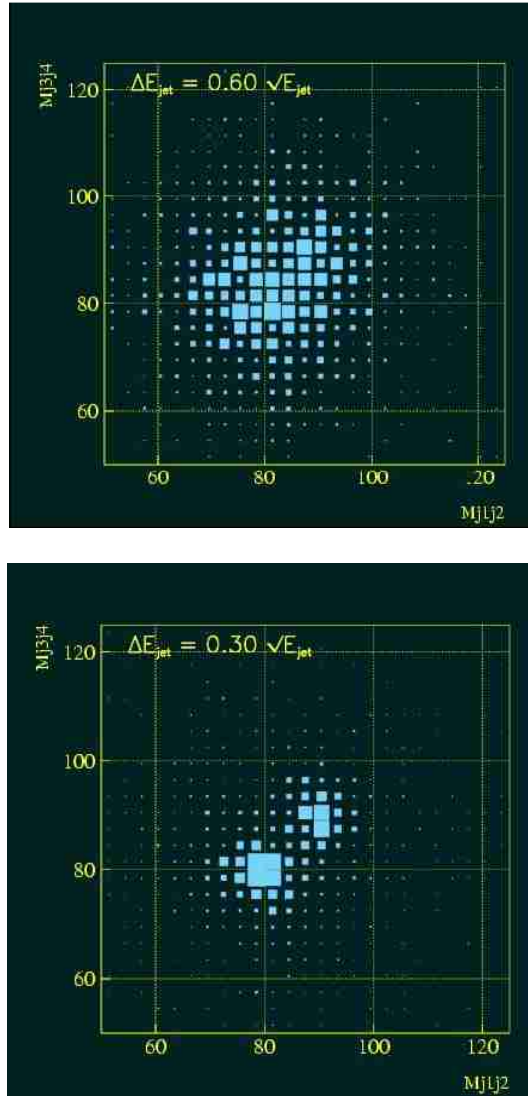


Figure 2.1: Relative improvement in separation of Z and W di-jet masses for jet resolution of 60% (top) and 30% (bottom).

CHAPTER 3

THE TAIL CATCHER/ MUON TRACKER

3.1 Introduction

The CALICE collaboration has developed a prototype detector for the ILC featuring three components, an electromagnetic calorimeter (ECAL), a hadron calorimeter (HCAL), and a Tail Catcher/Muon Tracker (TCMT) as shown in Fig. 3.1. The beam arrives from the lower left corner of the figure striking the small square ECAL with the black forward surface and silver/gray sides. The ECAL measures the energy of particles that interact electromagnetically. Behind the ECAL is the cubic meter HCAL covered with black cables in the photo. The HCAL measures the energy of particles that interact via the strong force. Behind the HCAL in the upper center part of the photo is the TCMT in blue with an orange frame. Data acquisition readout electronics are contained in the silver/white equipment racks in the lower center part of the photograph.

The CALICE Tail Catcher/Muon Tracker serves as a prototype ILC muon detector using SiPMs and offers an opportunity to study and correct for leakage in the case of thin hadronic calorimetry. These studies require test beam data to study the hadronic shower structure and validate available simulations, understand and address the

impact of a magnetic coil between the HCAL and TCMT, understand the TCMT in the PFA framework, and achieve good muon identification with acceptable fake rates.

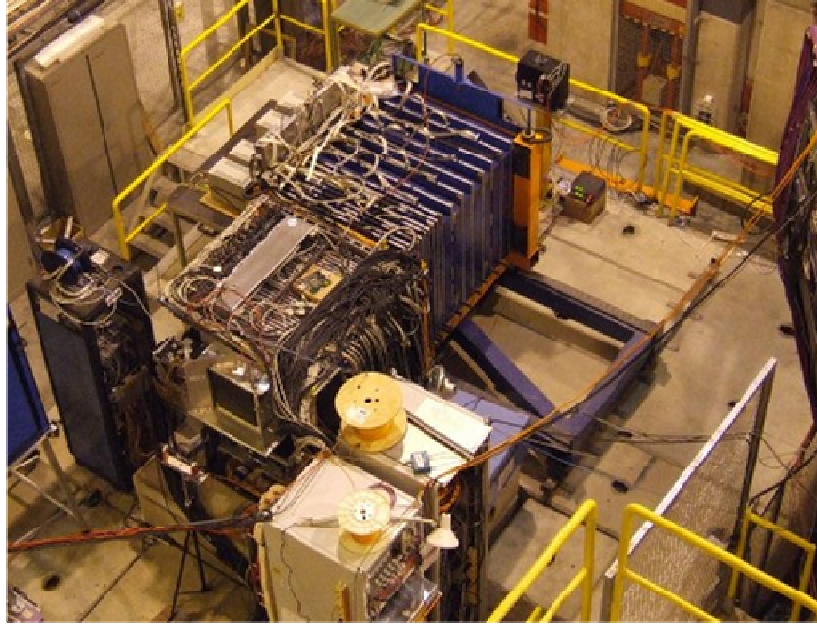


Figure 3.1: CALICE detectors at CERN test beam 2006.

3.2 Design Motivations

The TCMT must be of sufficient depth to contain hadronic showers and validate Monte Carlos for PFA studies. GEANT4 simulations using the SiD ECAL and HCAL design were used to select some of the design parameters including the thickness and width of the strips, number of active layers, and the thickness of the active layers. The

eight 1.9 cm absorber plates in the thin section were selected to be close to the 1.6cm thicknesses of the HCAL absorbers and to yield an additional nuclear interaction length of depth to the calorimeter system.

3.3 Mechanical Structure/Absorber

As shown in Fig. 3.2, the TCMT has two sections, a “fine” section with eight layers of 1.9 cm thick steel absorber selected to be as close to the same thickness as the HCAL with available materials and a “coarse” section with eight layers of 10.2 cm thick steel. The mechanical structure and absorber stack were engineered and assembled by the Fermi National Accelerator Laboratory Particle Physics Division. The TCMT mechanical structure has a length (along the beam) of 142 cm, a height of 109 cm, and a weight of approximately 10 tons. It has a total nuclear interaction length of 5.5λ .

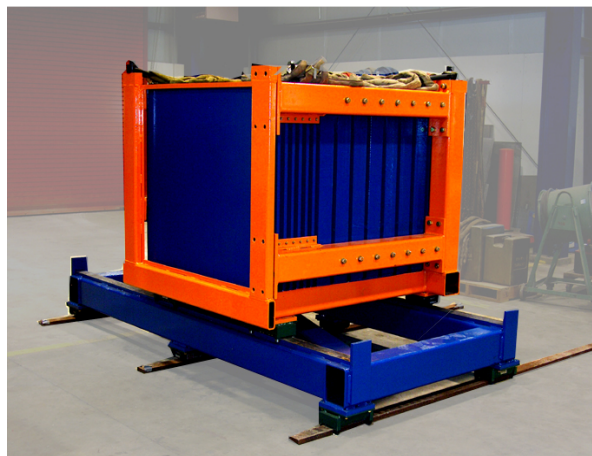


Figure 3.2: TCMT absorber structure showing fine and coarse sections.

3.4 Active Layers

The scintillator forming the active medium between the absorber plates are assembled inside 16 “cassettes” or modules. Each cassette houses 20 extruded scintillator strips that are 5 mm thick and 5 cm wide, and therefore the TCMT includes 320 strips. Fig. 3.3 shows the TCMT complement of scintillator segments after final machining. These segments were manufactured at the Fermilab/NICADD extruder facility with an original width of 10 cm, a length of 110 cm, and with two 2 mm co-extruded holes or channels running the length of the plate. The channels were 2.5 cm from each side. In the next step, a groove approximately 1 m long was cut down the center of each segment so that about 5 cm remained between the end of the groove and the edge of the scintillator. The groove was filled with a reflective white epoxy made of DER 332 epoxy and Jeffamine. This separation groove made the two parts separate, optically isolated, 5cm wide strips. The ends of each segment were removed leaving a 1 m long element. Each segment was therefore two strips glued together.



Figure 3.3: Extruded scintillator segments.

Before installation in the cassettes all the scintillator was tested in a light tight box with a fiber 110 cm long, a photo-multiplier tube (PMT) and a signal generated by a Strontium-90 radiation source. As noted earlier the strips were produced in pairs from a segment of scintillator. To select the best segments (strip pairs) for further processing five main criteria were used to ensure reasonable uniformity of response for all strips. The first criteria required that the average of five measurement points on the strip (at 90, 80, 50, 20, and 10 cm from the edge nearest the PMT sensor) be greater than 90% of a reference cell measurement. The second criteria required that the ratio of the average response of the two strips of the segment be within ± 2 sigma of the mean for the batch of strips. The third criteria required that the ratio of the measurements at the 20 and 80 cm points be within ± 2 sigma of the mean of the batch of strips. The fourth criteria required that the ratio of the 10 cm to 90 cm measurements be within ± 2 sigma of the

mean of the batch of strips. The fifth criteria required that the ratio of the 10 cm to 20 cm measurements be within ± 2 sigma of the mean of the batch of strips. Using the above criteria 227 out of 288 segments manufactured were considered acceptable.

Light can leak out surfaces of the scintillator leading to a poor signal. To improve the signal response two techniques were used to reflect light back into the scintillator. First, the outer edges of the segments were painted with a reflective white paint, EJ-510 from Eljen Technology. Second, the top and bottom surfaces were covered with a reflective material. For most of the strips two layers of Tyvek, a white, reflective insulator, were used on the top and bottom layers.

The farther light has to travel through the scintillator before it reaches the photo-sensor the weaker the signal. This effect is called attenuation. Preliminary measurements using the radiation source gave attenuations on the order of 20-25% from the near end of the strip to the far end. Using VM-2000, a more reflective material than Tyvek, covering part of the strip farthest from the sensor the attenuation can be reduced to around 10%. As these measurements were performed in conditions somewhat different from the actual installation of the strips in the cassette at the test beam, they should be taken only as a relative indication that attenuation can be compensated for by adjusting the reflective material along the length of the strip. Only enough VM-2000 material was available to apply the technique to five of the cassettes. For these cassettes, 30 cm of VM-2000 was added to the bottom of the strip farthest from the sensor and 20 cm of VM-2000 was added to the top of the strip. (These were cassettes 1 to 5 installed as layers 1, 2, 3, 5, and

7). Measurements of attenuation from test beam data indicated an average attenuation around 10% over the length of the strip [16].

As shown in Fig. 3.4, strips were installed in each 1 m x 1 m cassette and covered with either Tyvek or VM2000 used as reflective materials to increase light yield. The cassettes were installed in the absorber stack in an alternating x-y orientation. Readout is through a 1.5 mm diameter green wavelength shifting (WLS) fiber with a polished and aluminized end. The fiber is inserted down the middle of each optically isolated strip in a channel located 2.5 cm from each strip edge. The fiber directs the light to a SiPM supplied by the Moscow Engineering and Physics Institute (MEPHI) in collaboration with the Pulsar Enterprise for light detection, see Fig. 3.5. The fiber is necessary to shift the blue light of scintillator down to a wavelength in the green part of the spectrum to which the SiPM is more sensitive. The TCMT is equipped with the same electronics used to read out the CALICE HCAL from DESY. The data acquisition (DAQ) was provided by Imperial College [17].

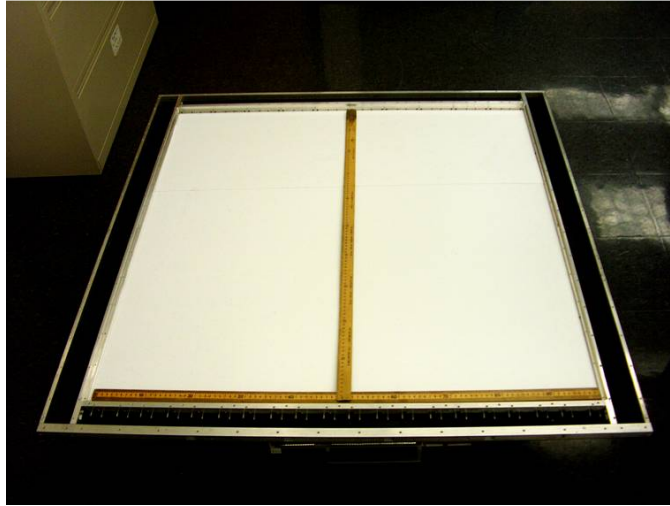


Figure 3.4: TCMT cassette frame.

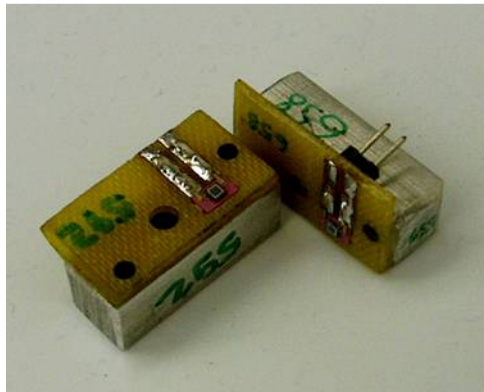


Figure 3.5: SiPM on holder.

The DAQ includes custom Linux software developed by the CALICE collaboration running on a PC controlling a VME DAQ board. The DAQ board connects to a base board which has up to six amplifiers. Each amplifier has 18 channels that can be set into one of two modes by software selecting from a set of resistors and capacitors. The two modes determine how the input pulse is shaped before being digitized by the analog to digital converter. One mode, called "physics mode," uses a stretched pulse of

around 180 ns with low gain and wide dynamic range and is for taking physics data during beam runs. The other mode, called "calibration mode," uses a shorter pulse of around 40 ns with higher gain and is used for the LED calibration measurements when the high gain is needed to determine the single photo-electron spectra for the gain and light yield measurements. Calibration mode has a shorted dynamic range and is more sensitive to noise and is therefore inappropriate for taking physics data. The gain ratio between the two modes varies between chips. The chips are in two populations one with the ratio around seven and the other with the ratio around 13.

The DAQ system includes a VME crate with slots for CALICE Readout Card (CRC). Each CRC supports eight front ends; each front end can connect to two base boards. Each base board has six amplifier/ADC chips which, in turn, have 18 channels. A total of two front ends, four base boards, 24 chips and 432 channels are reserved for the TCMT. Only 320 channels are required.

Each strip has a light emitting diode (LED) for calibration purposes. The LED is controlled by a LED driver circuit installed in a cassette panel opposite the SiPM sensors. The LED driver allows for the setting of LED amplitude by the DAQ system. The LED has three main functions. The first is to enable gain calibration of each channel. The ADC is placed in calibration mode and the amplitude of the LED is set low to detect the photo-electron spectra of the channel. Separation of the individual photo-electron peaks gives the gain of the channel in ADC counts per photo-electron.

The second function of the LED is to enable calculation of the ratio between calibration and physics modes of the ADC channel by measuring the response of the

channel to the same, high LED amplitude, but in both modes. The third main function of the LED driver is to study the stability of the system by periodically taking LED data at fixed LED amplitude in physics mode.

Each TCMT cassette has a 20 channel LED driver board. Every four cassettes are connected to a custom fanout board (a total of four needed for the entire TCMT) each with an independent power supply. For the October 2006 data taking run, the fanout boards were produced in two different configurations that required slightly different LED amplitude settings. Details of the results of the LED calibration functions will be discussed in a separate chapter.

3.5 TCMT with CALICE Calorimeters at the CERN Test Beam

The TCMT is designed to be used in conjunction with the CALICE ECAL and HCAL and other detectors for particle ID and triggering. The ECAL design has:

- 30 active layers of silicon diode pad detectors with ~10,000 channels
- 30 x 30 cm area incident to beam
- tungsten absorbers with thickness from 1.4 mm to 4.2 mm
- total thickness $24 X_0$ (radiation lengths)

The HCAL design has:

- 38 active layers each with 3 cm, 6 cm and 12 cm square cells
- 38 absorbers with 1.6 cm thick stainless steel plates
- total thickness of 4.5λ (interaction lengths)

This dissertation focuses on data taken in October 2006. At that time, the ECAL and HCAL were not completely instrumented and instead had the following configurations

ECAL:

- in each plane six out of nine sensor pads in place, the 30 square cm is built out of nine
- sensor pads in a 3x3 configuration. The lowest row of three pads was not installed in 2006 resulting in a 30 x 20 cm functional surface incident to the beam

HCAL:

- 30 out of 38 absorbers in place
- Layers 1-17 - all instrumented
- Layers 19-29 - every other layer instrumented
- a total of 23 layers x 216 channels/layer = 4968 channels

During the 2006 run period, the TCMT was fully instrumented with strips and SiPMs. Two layers did not have a functional LED which prevented some calibration data from being collected for the associated strips. Fig. 3.6 shows the TCMT electronics and cabling from the 2007 run period.

Figure 3.7 shows how the sections of the ECAL, HCAL and TCMT are arranged, their relative position, and thickness in nuclear interaction lengths. Fig 3.8 [18] shows the location and spacing of the HCAL active and absorber layers. Fig. 3.9 shows the TCMT active and absorber layers.



Figure 3.6: TCMT fully instrumented at CERN test beam 2007.

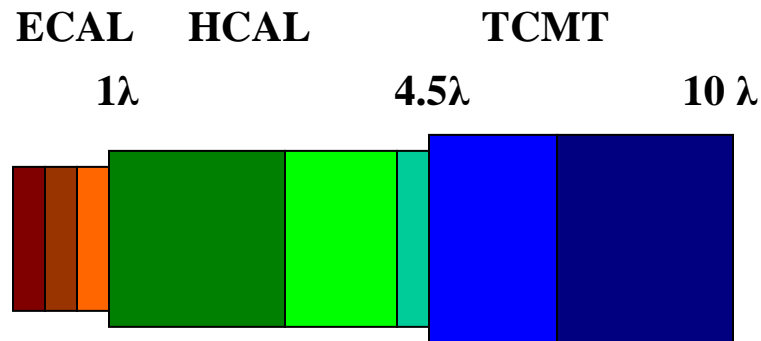


Figure 3.7: Diagram of the CALICE detector in October 2006 showing main sections. Red, brown and orange are the SiW ECAL segments. Dark green represents the HCAL forward section with 17 fully instrumented layers. Light green represents the HCAL rear section with six active layers placed after every other absorber. Blue/green represents the last two absorbers of HCAL. Light blue represents the eight TCMT layers with thin absorber. Dark blue represents the eight TCMT layers with thick absorber.

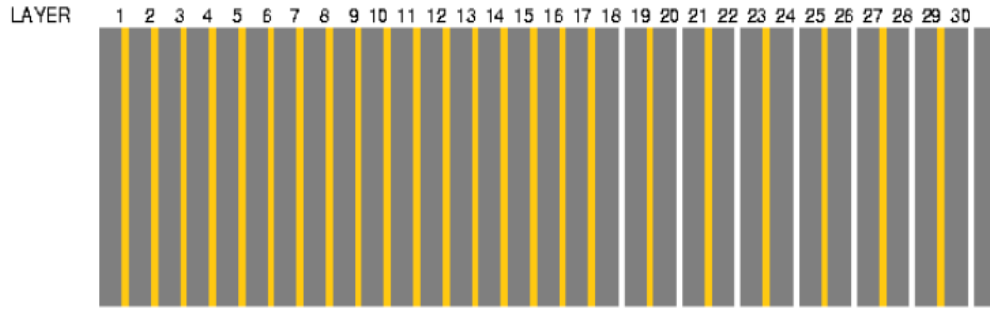


Figure 3.8: Diagram of CALICE HCAL during the October 2006 CERN run period showing the order of absorber (gray) and active layers (yellow).

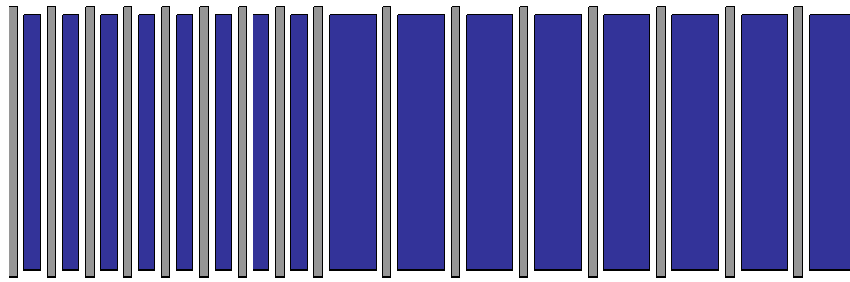


Figure 3.9: Diagram of CALICE TCMT showing the order of active layers (gray) and absorber layers (blue) of two different thicknesses.

This analysis compares 30 different hardware configurations. Seventeen configurations are simply extensions of the calorimeter by adding zero to 16 layers of the TCMT to the ECAL and HCAL calorimeters, more tersely:

$$\text{ECAL} + \text{HCAL} + n \text{ layers of TCMT where } n=0 \text{ to } 16 .$$

Thirteen additional configurations simulate the impact of an 1.8λ magnetic coil with additional sampling layers before and after the simulated coils:

$$\text{ECAL} + \text{HCAL} + n \text{ layers of TCMT} + 1.8 \lambda \text{ coil gap} + \text{remaining layers of TCMT}$$

where $n = 0$ to 6. In the following text and plots the index “ n ” in the two expressions are taken to be equal. For the coil simulations the sampling weight (to be described later) of the first active layer was re-calculated to compensate for the 1.8λ absorber corresponding to the coil.

Table 3.1 shows the specific allocation of the TCMT layers in this analysis. The second column indicates how many forward layers of the TCMT are added to the ECAL and HCAL to form the 13 different calorimeter configurations used to study the effect of varying the HCAL depth. To study the improvements in energy resolution due to the addition of a tail catcher outside a coil, columns three to five show the way in which TCMT layers are used as passive coil material or as active layers for post-coil sampling. (The four additional configurations corresponding to adding TCMT layers 0-13, 0-14, 0-15, and 0-16 are omitted from the table).

For example, Configuration 3 has two TCMT layers added to the calorimeter, nine skipped layers to emulate the coil and five layers for post-coil sampling (note that the first TCMT layer is numbered 0). This can be seen graphically in Fig. 3.10 where the sections are highlighted in red, gray and blue respectively.

Table 3.1. TCMT Layers Used for Analysis

Configuration number	# TCMT layers, n , added to HCAL (thickness in λ)	Parameters for “with coil” study		
		“coil” thickness (λ)	First layer # of TCMT for post coil sampling	# TCMT layers, m , for post-coil sampling (thickness in λ)
1	0 (4.54)	1.78	10	6 (3.74)
2	1 (4.79)	1.59	10	6 (3.74)
3	2 (4.90)	2.08	11	5 (3.12)
4	3 (5.02)	1.96	11	5 (3.12)
5	4 (5.14)	1.83	11	5 (3.12)
6	5 (5.25)	1.71	11	5 (3.12)
7	6 (5.37)	1.59	11	5 (3.12)
8	7 (5.49)	2.08	12	4 (2.49)
9	8 (5.60)	1.96	12	4 (2.49)
10	9 (5.72)	1.83	12	4 (2.49)
11	10 (6.34)	1.83	13	3 (1.87)
12	11 (6.96)	1.83	14	2 (1.25)
13	12 (7.59)	1.83	15	1 (0.62)

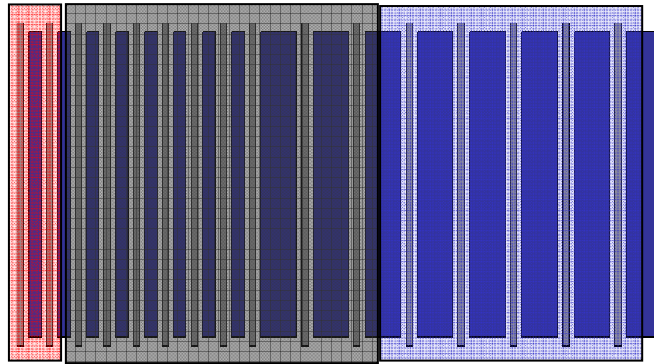


Figure 3.10: Diagram of TCMT for example Configuration 3. The front two layers (highlighted in red) are treated as additional layers of the hadronic calorimeter. The next nine layers (highlighted in gray) are omitted from the analysis to simulate a coil of approximately 1.8 interaction lengths. The final five layers of the TCMT (highlighted in blue) are treated as post coil sampling.

CHAPTER 4

CALICE INSTALLATION AT THE CERN TEST BEAM

In August 2006 the TCMT was installed with the ECAL and HCAL at the H6 beam line at the SPS north area at CERN, Fig.4.1 [19]. This thesis is focused on the October 2006 data, details of the October configuration will be discussed here. The CALICE installation at the CERN test beam includes the ECAL [20], HCAL [21], TCMT and numerous other detectors to trigger and identify and track particles (see Fig. 4.2 [22]).

The CERN complex contains many accelerators some acting as boosters for the next higher energy machine. The chain leading to the H6 beam line includes a linear accelerator, a booster, the proton synchrotron (PS), and the super proton synchrotron (SPS).

The primary beam from the SPS is a proton beam of up to 400 GeV. The beam is directed on a fixed target producing a beam of secondary particles. The beam that reached the CALICE detector contains a mix of protons, electrons, pions and muons. Tuning magnets, collimators and absorbers were selected and adjusted from the control room to determine beam momentum, particle species and electric charge. The beam cannot be completely pure but additional detectors such as Cherenkov detectors or a muon veto counter can be used to identify events with or without the desired particle.

CERN Accelerator Complex

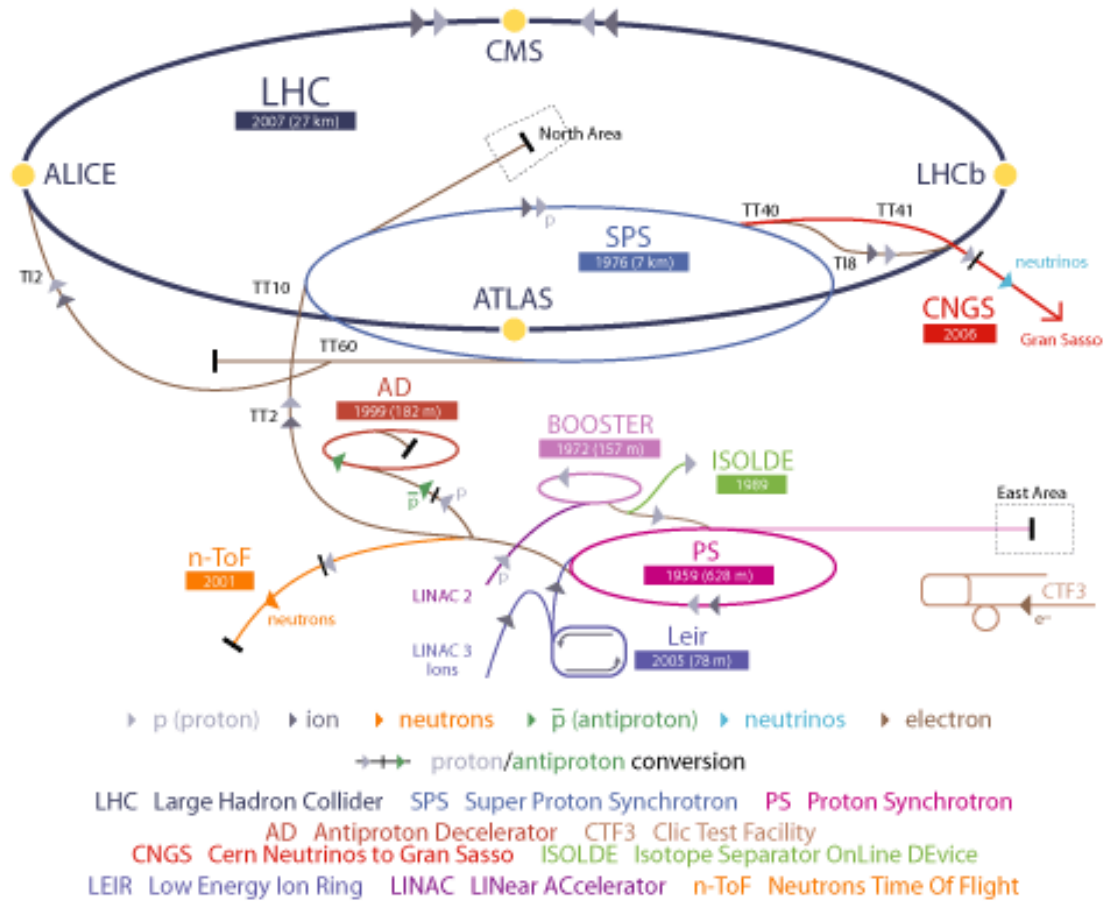


Figure 4.1: Diagram of CERN accelerator complex.

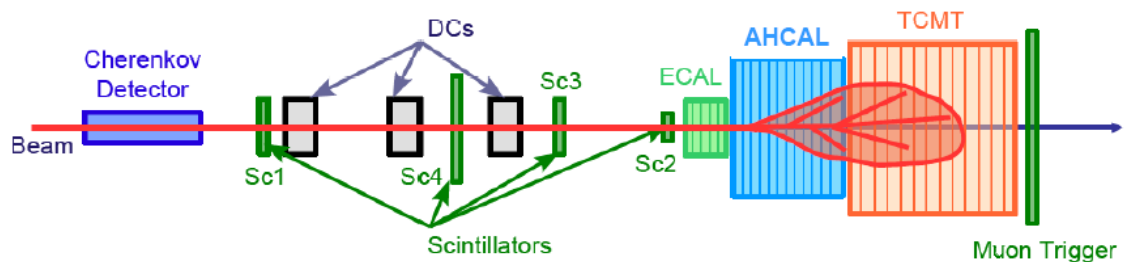


Figure 4.2: Block diagram of CALICE detectors at CERN 2006 test beam with an example schematic hadron shower in the HCAL extending into TCMT.

Table 4.1 [23] describes the pion runs taken, their energies, polarity and approximate number of events. Electron runs were also taken but since electrons do not penetrate to the TCMT they are not considered in the following analysis. Approximately 9.5M muon events were also collected. Although, a beam run had a dominant particle species, contamination was present. For example, a 20 GeV negative pion run can be contaminated by approximately 19% non-pion events. Muon counters and Cherenkov detectors are used to eliminate contamination.

Table 4.1 Calibrated Run List for Pions

Beam Momentum (GeV)	π^+ (kEvents)	π^- (kEvents)
6	450	1400
8		1300
10	700	1800
12		1200
15	700	1600
18		1300
20	800	1500
30	800	
40	800	
50	1300	
80	1300	

The Cherenkov detector uses the Cherenkov effect in which charged particles with a speed exceeding the speed of light in the material produce light. Thus each medium has a velocity threshold, below which a particle will not produce any Cherenkov light. If the medium is a gas, the pressure can be adjusted to change the density and thus

the speed of light, and so the threshold velocity. Two different species of particle with the same momentum but with different mass will have different velocities. One will emit light, the second will not. Through this technique the velocity and, therefore, the mass or species of the particle can be selected. In the case of the CERN configuration, the Cherenkov detector was filled with helium gas and used to select between pions and electrons when the beam energy was less than 40 GeV. For higher energies it was filled with nitrogen gas and used to select between protons and pions. The efficiency ranged from 90% at the optimal setting to 30% [24]. Fig. 4.3 [25] shows an example response of the Cherenkov detector as a function of pressure, in bars, during an 80 GeV pion beam. The number of proton events per spill is plotted. The line at 0.15 bar indicated the selected pressure to detect protons for 80 GeV runs. The use of the Cherenkov detector to purify the event sample is discussed in Chapter 7.

Triggering for each event was accomplished with four scintillation counters constructed with a strip of plastic scintillating material connected to a photomultiplier tube. The counters give an analog signal that was later digitized. The event trigger required a coincidence of two out of three scintillation counters, Sc1 (100x100 mm), Sc2 (30x30 mm) or Sc3 (100x100 mm) as labeled in the block diagram. The larger counter Sc4 (200x200 mm) in anti-coincidence with Sc1 and Sc3 was also used to veto beam halo offline. The analog output of the scintillation counters can be used as an indication of multi-particle events offline.

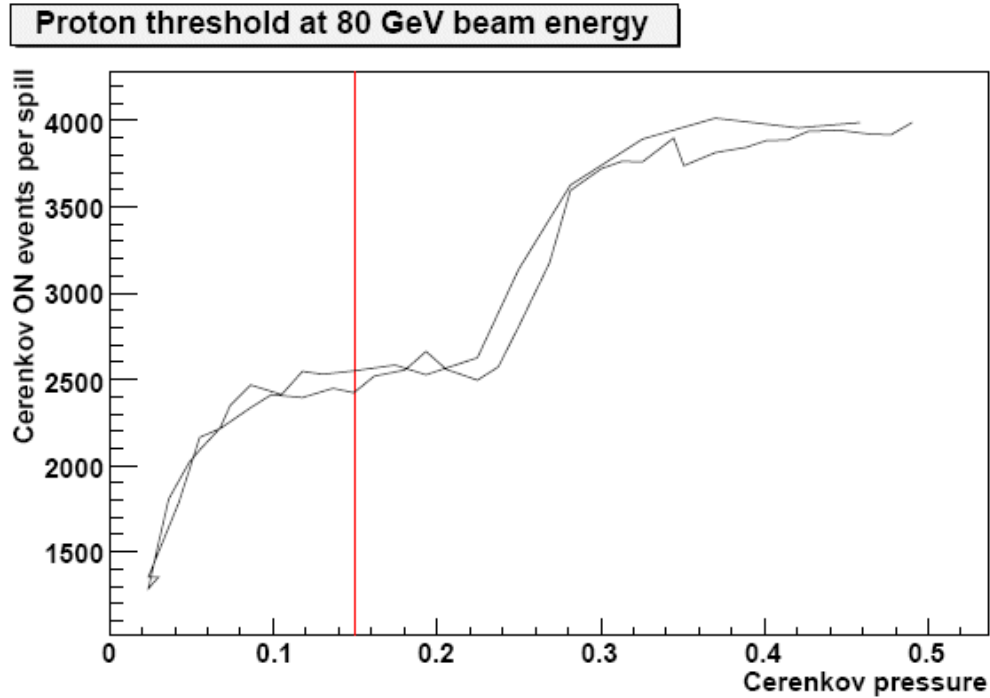


Figure 4.3: Example response of the Cherenkov detector as a function of pressure in an 80 GeV pion beam. (Pressure is given in bars. Cherenkov ON events correspond to the number of protons detected.)

To monitor the beam, identify the beam impact point on the ECAL, and reconstruct tracks three x/y pairs of delay wire chambers (DWC) were used. They are designated DC1, DC2, and DC3. The DWCs are filled with a gas that ionizes with the passage of a charged particle. The chamber has anode and cathode wires at high voltage. Electrons liberated due to ionization drift with a known velocity to the anode wires and register a signal in the cathode wires. The timing between the event trigger and the registration of the signal can be used to calculate the location of the particle in the chamber. The DWCs are similar to multi-wire proportional chambers (MWPC) except

that in the WMPCs the signal is read out through the anode wires. Spatial resolution was on the order of $200\mu\text{m}$ [26].

A $1\text{ m} \times 1\text{ m}$ scintillator counter located behind the TMCT, designated Mc1, was used to identify muons. Most non-muons will have been absorbed in the >10 nuclear interaction lengths of the ECAL, HCAL and TCMT. Any positive signal in Mc1 is most likely a muon. This can be used for triggering on muons for muon calibration or offline processing to veto muons from pion runs. Fig. 4.4 [27] indicates spacing details between detectors.

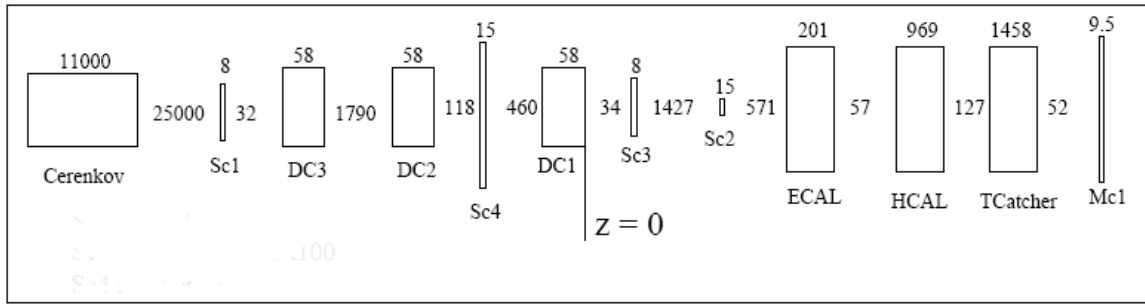


Figure 4.4: Detailed spacing diagram of CALICE detectors. All dimensions are in mm. (Not to scale.)

Data from each run was recorded in a series of data files containing up to 200k events each. Each run was stored as a series of data record configurations. Every ten minutes a 500 event pedestal configuration was taken to monitor pedestal stability. The pedestal configuration was followed by a 500 event LED calibration configuration used to monitor the gain of the sensors. Details of the pedestal and LED calibration data are

discussed in Chapter 5. The other configurations contain beam triggered particle events. Each event record contains data organized by VME crate, slot number, front end, chip and channel. The 320 TCMT data channels were contained in two front ends of one slot of the HCAL VME crate.

CHAPTER 5

CALIBRATION AND STABILITY

5.1 Introduction

The calibration of the TCMT channels was accomplished with a LED system and with muon runs. The device stability was monitored using pedestal runs and inter-spill pedestal configurations. In this chapter the gain, light yield, MIP calibration values and pedestal stability are discussed.

5.2 SiPM Gain Determination

As described in the chapter on the construction of the TCMT, each strip has an ultraviolet LED at the end opposite the sensor. The DAQ controlled the brightness of the LED by controlling the current supplied to the LED through a LED driver board. One 20 channel driver board was installed in each cassette. A fanout board supplied power and control signals to four LED driver boards. The amplifier calibration mode was selected to achieve a high gain and a LED brightness was selected to be low enough to generate a signal in which single photoelectron peaks could be discerned in the spectra. The separation of peaks is the gain of the channel in ADC counts.

The original design of the LED system included a computer controlled “trimDAC,” a circuit to set an analog output from a computer supplied digital input, to finely control the current and therefore brightness of each LED. This system did not function correctly so the brightness level had to be selected by trial and error. Because of this many channels had LED brightness that were either too high or too low to acquire the necessary photoelectron peaks.

A higher amplitude LED setting was used for mode-to-mode intercalibration measurements and long term stability studies. This level also had to be set by trial and error and had to be bright enough to yield a good signal in physics mode but not so bright as to saturation ADC while in calibration mode setting. The calibration mode to physics mode ratio is in the range of 7 to 13 depending on the individual analog to digital conversion integrated circuit chip and production run.

Figure 5.1 shows a typical photoelectron spectrum for one strip (or channel) of the TCMT. An automated peak finding algorithm located peaks in the spectrum, and the first two were subsequently fit with Gaussians. The first identifiable peak is usually the pedestal for that channel. This is confirmed by comparing to dedicated pedestal runs. The pedestal is the output of channel when no signal is applied. The pedestal peak is usually a Poisson distribution but due to large statistics a Gaussian fit is acceptably accurate. Each channel has a unique pedestal. The second peak is due to single photon illumination. The separation of the peaks equals the gain in ADC counts for that particular channel. Approximately 50% of the strip spectra could be fit through this automated technique. An additional 10% were recovered with manual intervention. Four cassettes did not have

functioning LED systems. The other strips that could not be fit either did not have functional SiPMs, did not have functioning LEDs or the LED were operating at a brightness that was too high to generate a spectrum with discernable peaks.

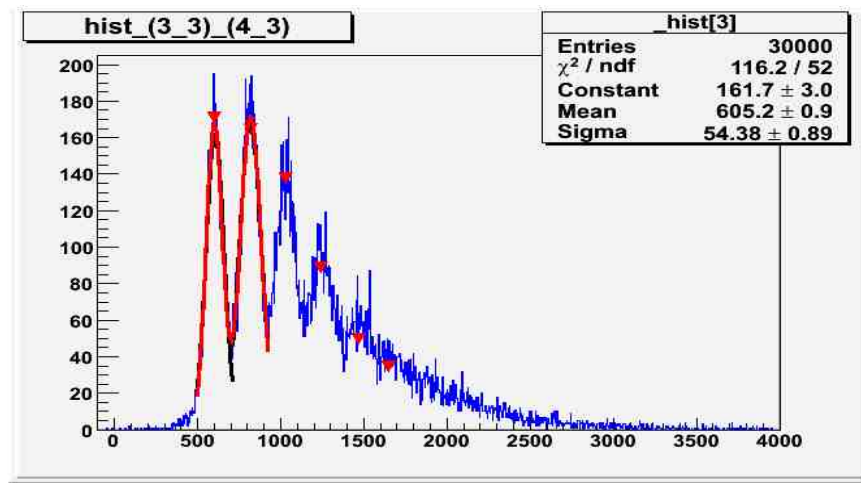


Figure 5.1: Typical photoelectron spectrum.

Figure 5.2 shows the distribution of gains for the 188 strip subset that could be fit. Data is from LED calibration tests taken during the commissioning period. The average gain is approximately 276 ADC counts per photon with an RMS of 79. Two peaks can be seen in this histogram. This is due to the fact that two different batches of SiPM were used. Cassettes 1 to 8 (layers 1 to 8) used one batch with an average gain of 336 and a

standard deviation of 61. Cassettes 9 to 16 (layers 9 to 16) used a different batch of SiPMs and have an average gain of 227 and a standard deviation of 56.

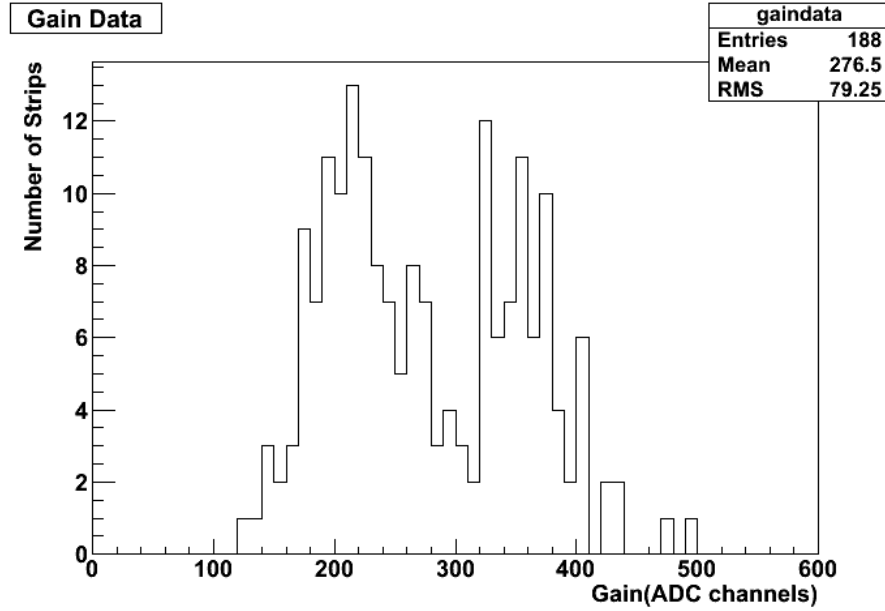


Figure 5.2: Distribution of gains.

The commissioning of the TCMT occurred in four phases. First the SiPM sensor output was integrated with the CALICE DAQ system at DESY in October of 2005. Next a prototype cassette with a separate DAQ was installed in the Fermilab Meson Test Beam Facility (MTBF) in February of 2006. This demonstrated the basic functionality of the cassette in a test beam environment. Third, as the LED driver boards became available they were installed in the cassettes and used to confirm that each strip was functional,

determine the general light level needed for maximum calibration signal, and determine the light level needed to obtain photo-electron spectra required for calibration.

The fourth phase occurred in two steps. SiPMs for eight of the 16 cassettes were available for an August 2006 run period at the H6 beam line at CERN. During this run period the TCMT with half of the needed cassettes was integrated with the ECAL and HCAL. Photo-electron spectra were collected to measure the gain of approximately one half of the channels/strips. Beam dump muon runs were collected to measure the MIP calibration values to be described in the next section.

A further eight cassettes were completed and installed for the October 2006 run period. Additional, photo-electron spectra and MIP calibration runs were collected as well as intercalibration data. The intercalibration runs were taken at the same LED illumination amplitude in both the physics mode and calibration mode.

5.3 MIP Calibration

The TCMT channels were calibrated using muon runs. The beam dump muons used are approximately minimum ionizing particles (MIPs). A MIP is an ionizing particle with an energy loss rate at a minimum. A MIP generates the same response throughout the entire detector. Any difference in the readout for a given strip/channel is due to properties of that strip/channel. A beam run using MIPs is used to determine relative calibration factors in terms of ADC counts for all the channels. Figure 5.3 shows the

energy spectrum of an example strip taken during a muon calibration run. The most likely response in ADC channels at this peak is the calibration value for the channel.

Muons calibration events were selected with a software triggering algorithm. A good hit is defined as being a signal if it is at least 2σ from the pedestal. A muon is selected if five out of six of the nearest strips in neighboring cassettes also have good hits. Whenever possible, three strips in front and three strips behind were tested [28].

Figure 5.4 is a histogram of MIP calibration values in ADC channels for all 320 strips. The mean is 228.9 with an RMS of 134.2. The eight strips in the zero bin are due to dead SiPMs. When analyzing pion or electron beam runs, the raw ADC count value is then divided by the MIP calibration value for each channel to get the energy in terms of MIPs.

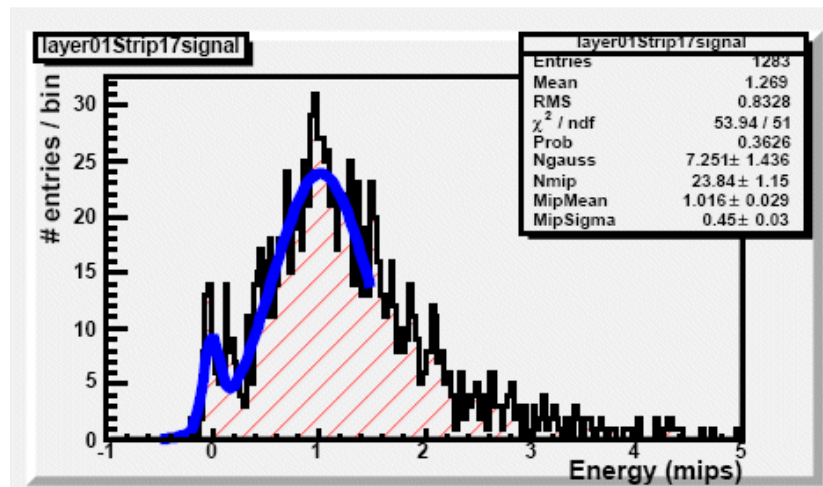


Figure 5.3: Example of MIP spectrum with Gaussian fit.

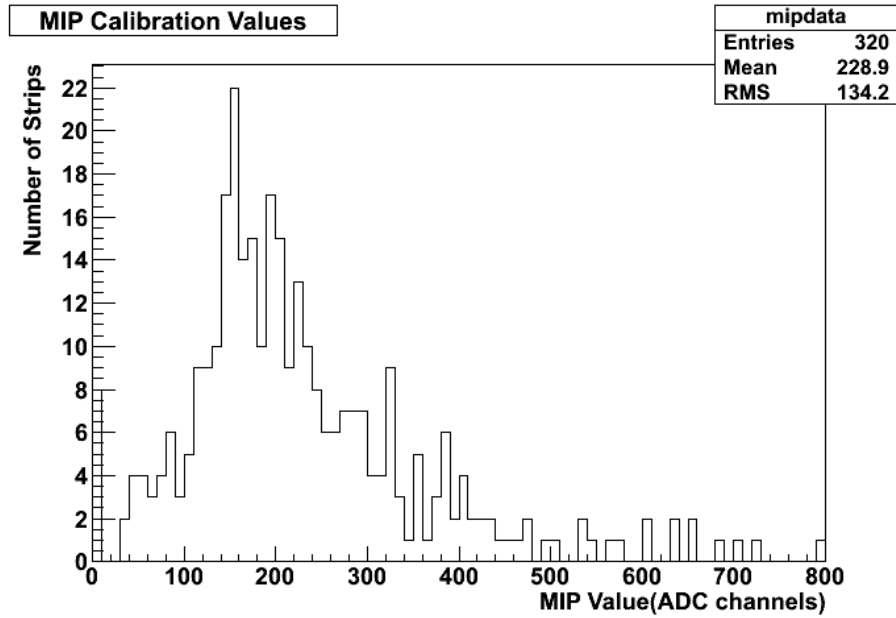


Figure 5.4: MIP calibration values.

5.4 Light Yield Determination

The gain in ADC counts and the MIP calibration values can be used to calculate the light yield in terms of photo-electrons per minimum ionizing particle (PE/MIP). The calibration mode to physics mode intercalibration factor is also required. The light yield can be calculated by the following equation:

$$LY. = \frac{1}{Gain} \times MF \times MIP$$

where Gain is the gain in ADC counts in calibration mode, MF is the calibration to physics mode factor, and MIP equals the ADC counts per MIP. For example, for layer 1, strip 3:

$$LY. = \frac{1P.E.}{197ADC.} \times 7.78 \times \frac{2465ADC.}{1M.I.P.} = 9.7P.E./M.I.P.$$

The LED system did not provide good gain data for many of the channels. In order to calculate the light yield the gain, intercalibration factor and MIP calibration value must be measured. All three of these values were only available for 135 channels, as shown in Fig 5.5. The mean light yield is 5.83 PE/MIP with an RMS of 1.69 PE/MIP.

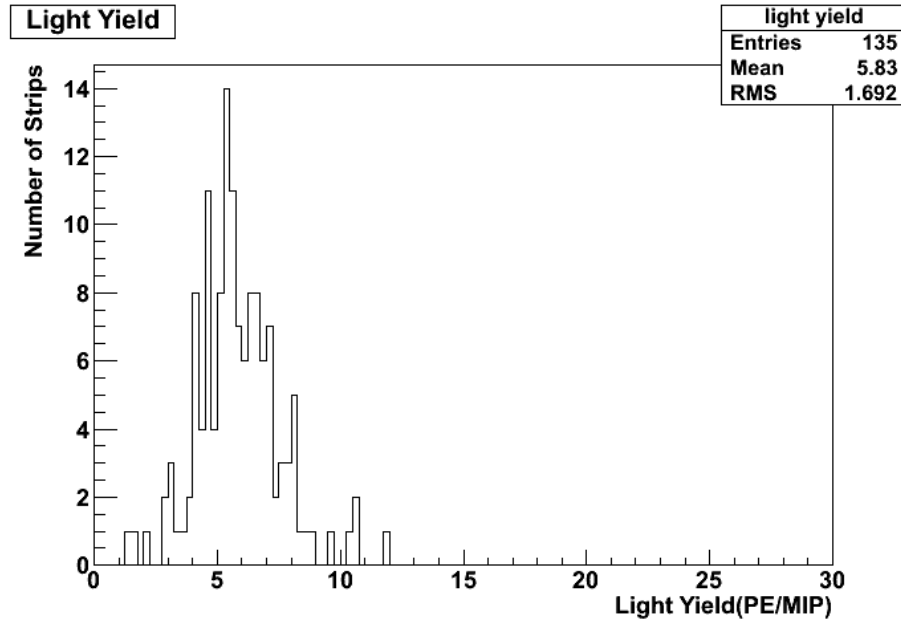


Figure 5.5: Calculated light yield for 135 TCMT strips.

To calculate the working light yield for all channels, the average gain of the available strips was used and the average intercalibration factor of available strips was

used to fill in most of the remaining strips. If the strip had a zero response from the MIP calibration value it was taken to be dead and assigned a light yield of zero. Fig. 5.6 is a histogram of the light yields actually used for the 313 functional strips. These values are used only for the saturation correction as described in Chapter 6.

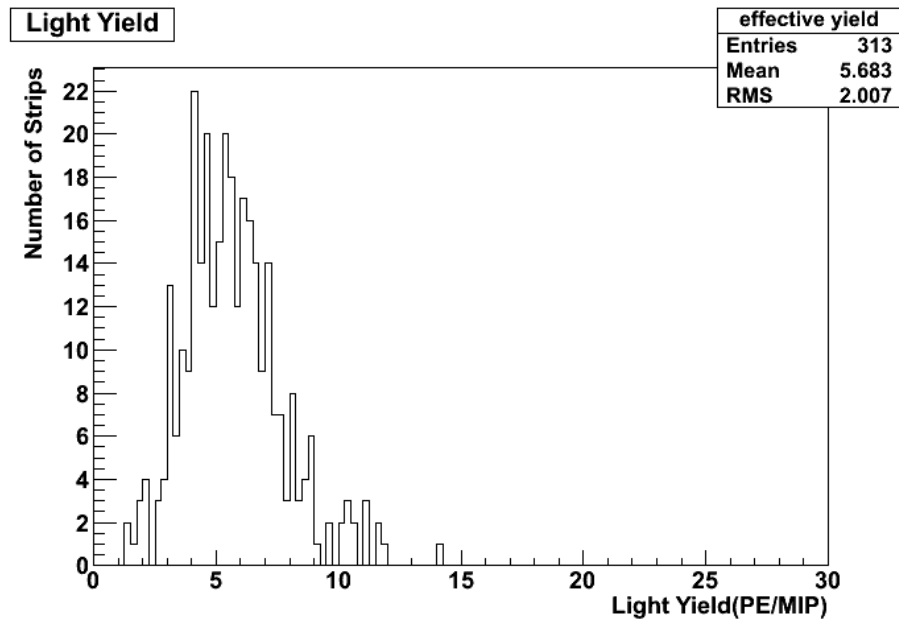


Figure 5.6: Effective light yield for working strips.

5.5 Pedestal Stability

Five hundred pedestal events were taken every ten minutes during beam runs. The stability of the pedestals can be analyzed by looking at these pedestal configurations between different runs. Figure 5.7 shows the percent change in the pedestals of one layer

between different runs taken over a 24 hour period. In the plot three subsequent runs are compared to the initial run. Between runs, the pedestals are stable to within approximately one percent. Fig. 5.8 shows the RMS change in pedestal counts for each layer between the four runs. The RMS change is the root mean square of the 20 channels of the layer.

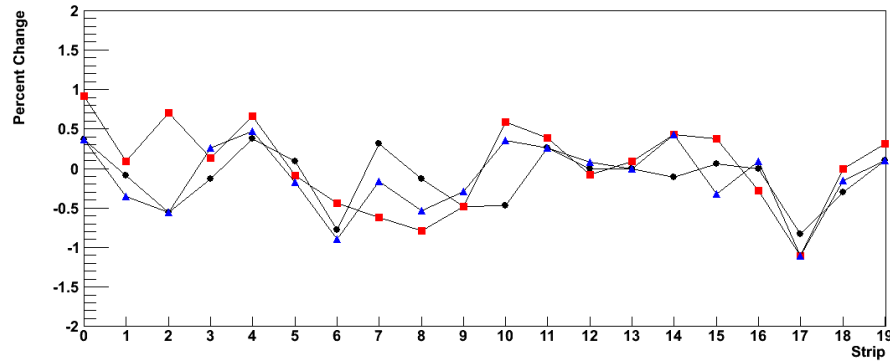


Figure 5.7: Percent change in pedestals of one layer between four different runs. (Circles: Run300631-Run300613, Squares: Run300643-Run300613, Triangles: Run300652-Run300613.)

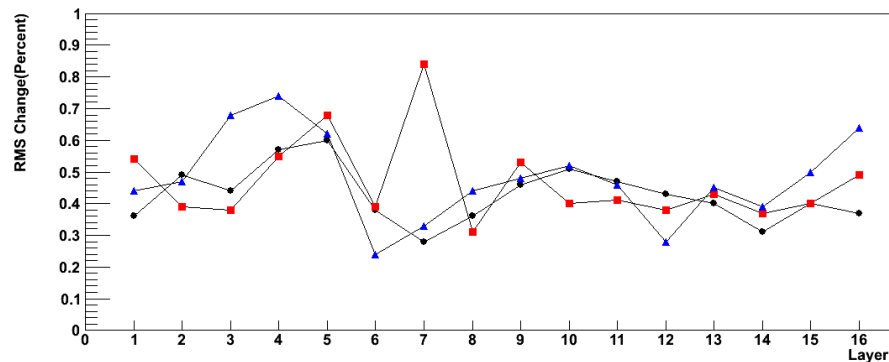


Figure 5.8: RMS change in pedestals (in ADC counts) for each layer between four runs. (Run300631-Run300613, Squares: Run300643-Run300613, Triangles: Run300652-Run300613.)

5.6 Temperature Effects and Preliminary Sampling Weights

Calibration steps are necessary to determine the correct ADC to MIP conversion, calculate a light yield, and monitor stability over time. The light yield in turn is necessary for calculations correcting SiPM saturation effects to be described in Chapter 6. The LED calibration system was not as effective as it could have been but did allow for accurate determination of gains in ADC counts for slightly more than half of the strips. The main reason the pedestal may drift would be due to SiPM temperature dependence. The stability of the pedestals over time, however, indicates that the temperature effects are small and have been neglected for the remainder of the analysis. Temperature change through each run is on the order of 1°C . In the HCAL, this typically translates to a 3.5% change in SiPM response [29]. Temperature monitoring and correction for the TCMT was not available in the run period but the response can be expected to be on the same order as the HCAL. Though this analysis would be enhanced by the addition of the temperature data, the use of a least squares fit to determine the sampling weights, to be described in Chapter 7, ameliorates the lack of temperature data to fully equalize the response of the individual strips due to temperature variations across the TCMT.

Intercalibration factors or weights need to be determined to take into account the response of different components of the CALICE calorimeter system. If the calorimeter is hermetic, all of the energy of the event will be contained but the energy distribution between each of the components will be different from event to event. The signals in the detector components will, however, be correlated.

Fig. 5.9 shows the correlation between the ECAL + HCAL total event energy and the TCMT total event energy. Events in which all of the event energy is contained in the ECAL and HCAL fall along the x axis and events in which all the energy is contained in the TCMT fall along the y axis. Ignoring resolution effects and punch through, the sum of the two components (treating ECAL and HCAL as one component and the TCMT as the second) must be equal and fall along a line. Statistical variation from event to event causes the data to spread out but a line can be drawn to estimate this correlation. The slope of the line can be used as a rough intercalibration factor that compensates for the different response of the two detector components. In this case the slope can be estimated at 0.9. This number then becomes an approximate weight to scale the TCMT response to equalize the calorimeter response. Once a weight can be assigned to each section the combined energy response of the three detectors can be determined. Reconstructed energy can then be reported in weighted MIPS.

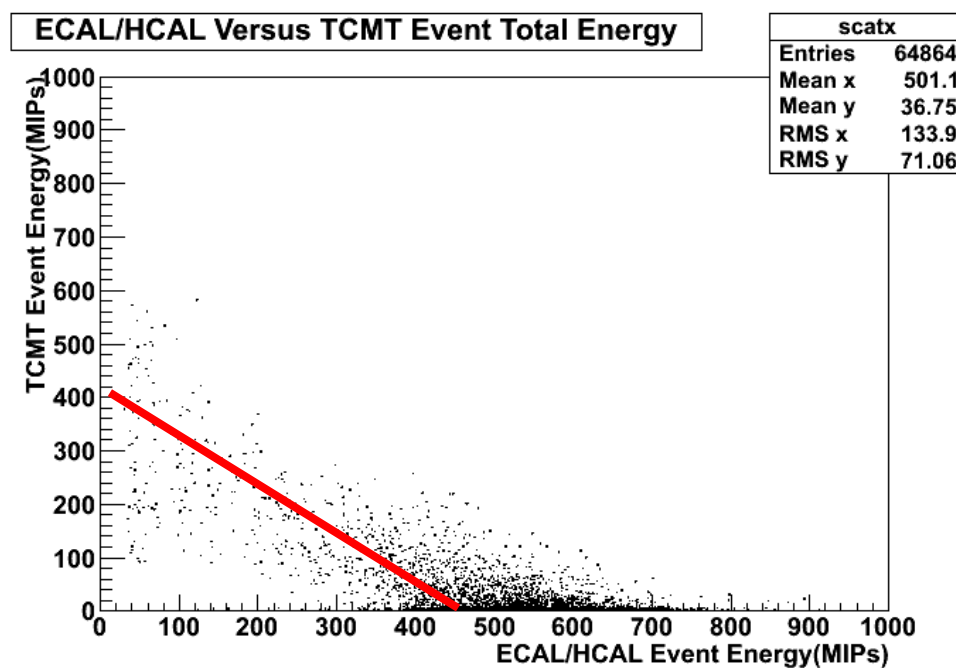


Figure 5.9: Correlation plot used to determine the intercalibration constant with a hand-drawn line estimating the correlation.

CHAPTER 6

STEPS TOWARD A CLEAN SAMPLE

6.1 Introduction

This analysis uses pion beam runs. Electron runs were also taken during the test beam but most of the electron energy is absorbed in the ECAL and HCAL. All the beam runs have a mixture of particles including pions, electrons and muons. Muons penetrate the entire detector system. To remove non-pion events from the analysis several separate requirements or “cuts” are used to prepare the analysis sample. The data was analyzed with a saturation correction applied to correct for the non-linear behavior of silicon photomultipliers.

6.2 Signal Threshold Cut

A signal threshold was applied to remove noise generated by the SiPMs. The threshold was determined using separate muon calibration runs. A 0.5 minimum ionizing particle (MIP) threshold was applied on each hit to reject noise.

6.3 Cuts Based on In-Beam Counters

Figure 6.1 shows the total energy spectrum with no cuts applied. The run is a 20 GeV negative pion run, the sample is contaminated by double particle events at high energy and muons and electrons at low energy. There is a sizable left side peak below 200 ADC counts due to these other particle species. The peak greatly skews the mean of the distribution to the low side and results in a high RMS.

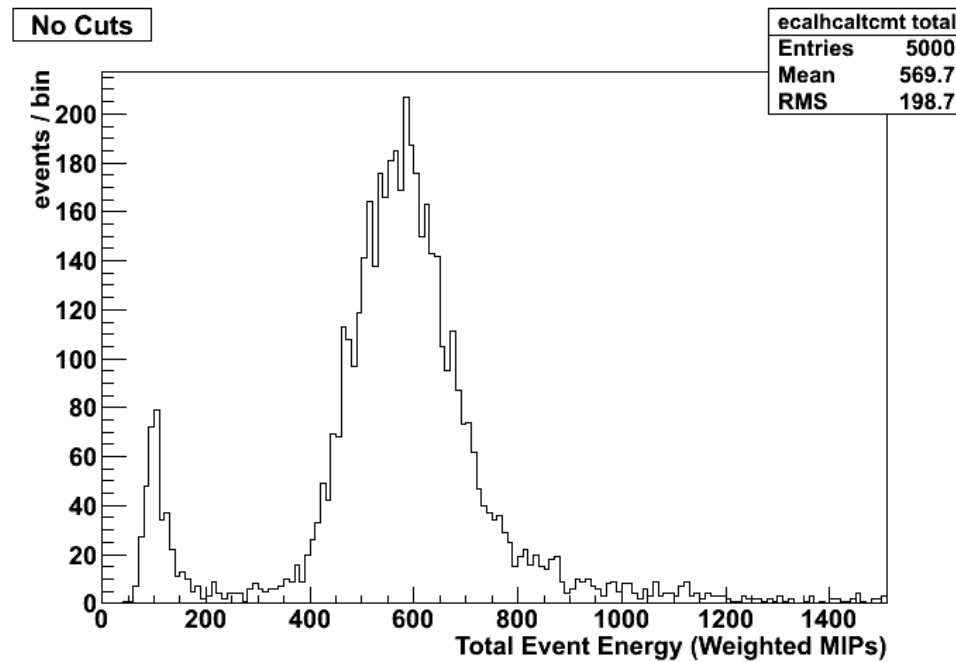


Figure 6.1: Energy spectrum for ECAL+HCAL+TCMT detector with no cuts.

Electrons are vetoed with the Cherenkov detector. Table 6.1 [30] gives the efficiency of the Cherenkov detector as a function of pressure. Fig. 6.2 shows the energy spectrum with the Cherenkov veto cut applied to remove electrons in a 20 GeV pion sample. The lower peak is greatly reduced.

Table 6.1 Cherenkov Electron Efficiency

energy	pressure	e ⁻ detection efficiency
15 GeV	1.35 bar	99%
20 GeV	0.76 bar	95%
30 GeV	0.338 bar	75%
40 GeV	0.190 bar	35%

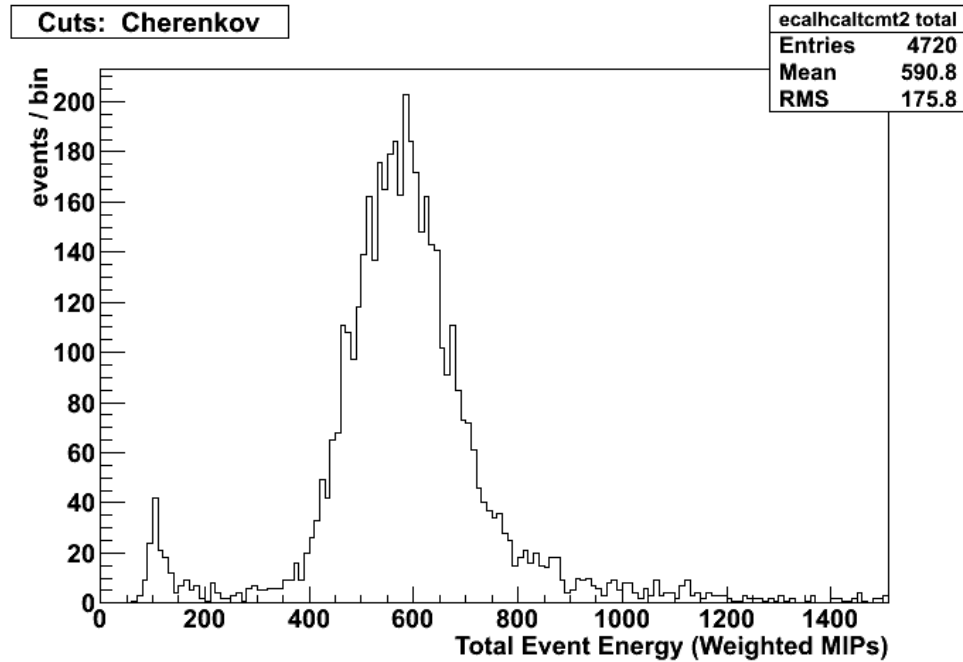


Figure 6.2: Energy spectrum for ECAL+HCAL+TCMT detector with Cherenkov detector cut to remove electrons.

Multi-particles are detected by observing the amplitude of the dedicated 20 cm x 20 cm veto scintillator located in front of the calorimeters. Fig 4.3 in Chapter 4 shows the location of the scintillators in the beam line. Most events are generated by a single particle. Some events may contain more than one particle. These events need to be rejected from the analysis because the additional particles would deposit excess energy in the detector. Fig 6.3 is the output of the veto counter. By inspection of the distribution there is a pedestal at approximately 1400 ADC counts and a MIP peak at 3000 ADC counts. A double particle event would have a peak at twice the separation or 4600 ADC counts. A small shoulder at this point can be seen in the figure. A threshold of 3800 ADC counts, half-way between the main peak and shoulder was selected to remove multi-particles. This is also consistent with other CALICE analysis efforts [31]. The effect of including multi-particle veto can be seen in Fig. 6.4.

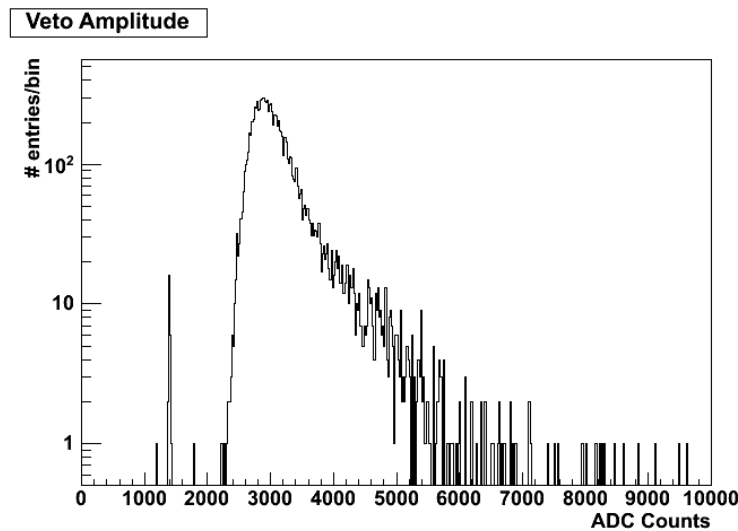


Figure 6.3: Veto counter amplitude.

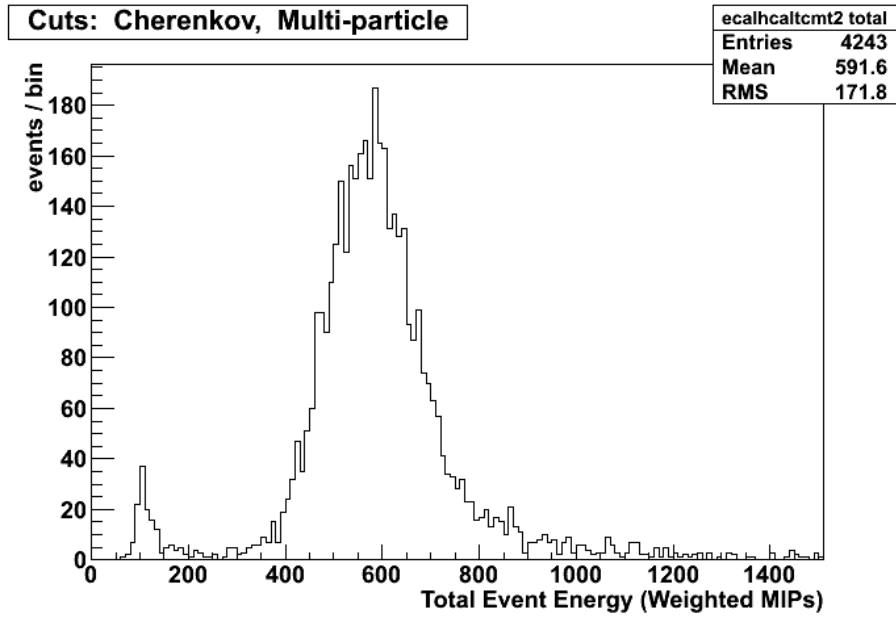


Figure 6.4: Energy spectrum for total detector with electron and multi-particle cuts applied.

Muons that penetrate the detector are detected by a 1 m x 1 m scintillator counter behind the TCMT. Fig. 6.5 shows the energy distribution when the double particle veto, electron and muon cuts are applied. There is a small but still significant tail under 200 ADC counts, presumably due to cut inefficiencies.

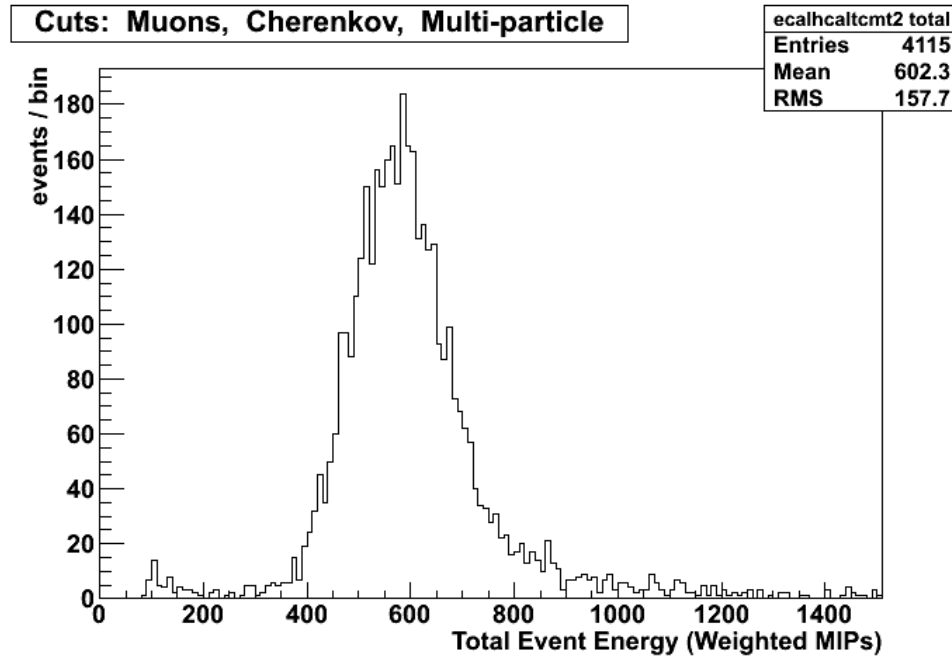


Figure 6.5: Energy spectrum of total detector with muon veto, electron and multi-particle cuts applied.

6.4 Energy to Hit Ratio Cut

Not all muons are vetoed by the 1m x 1m scintillator behind the TCMT. An additional technique to identify muons was developed by examining the energy deposition of beam dump muons. For muons, the ratio of event energy to number of hits should be close to one MIP per hit because beam dump muons are minimum ionizing particles. Fig. 6.6 plots the event energy to hit ratio for the three detectors: ECAL, HCAL, and TCMT. The histogram represents the subset of events which triggered the muon detector behind the TCMT. The ECAL and HCAL histograms have two peaks. The

low ratio peaks are due to events in which the particle missed completely or only grazed some of the layers the ECAL because of the ECAL smaller surface area. As the plots demonstrate, a muon can be selected by event energy to hit ratios for all three detectors. The actual threshold is specific to each detector and is selected by inspection from the plots in Fig. 6.6. The ratios used are:

ECAL: >1 MIP/hit,

HCAL: >2.5 MIP/hit,

TCMT: >2.5 MIP/hit.

Studies with Monte Carlo muon simulation were also performed and the results were consistent with the above thresholds.

Of the 5000 events in the muon sample, 2538 were tagged as muons by the muon counter behind the TCMT. These were used to test the efficiency of the energy to hit ratio cut. Table 6.2 gives the efficiency of the ratio cut detecting muons for events tagged by the muon counter for individual sub-detector (ECAL, HCAL and TCMT) and for the complete CALICE detector system such that all three sub-detectors simultaneously detect a muon. Fig. 6.7 shows the event total energy spectrum with all cuts applied. Note the low tail is nearly gone.

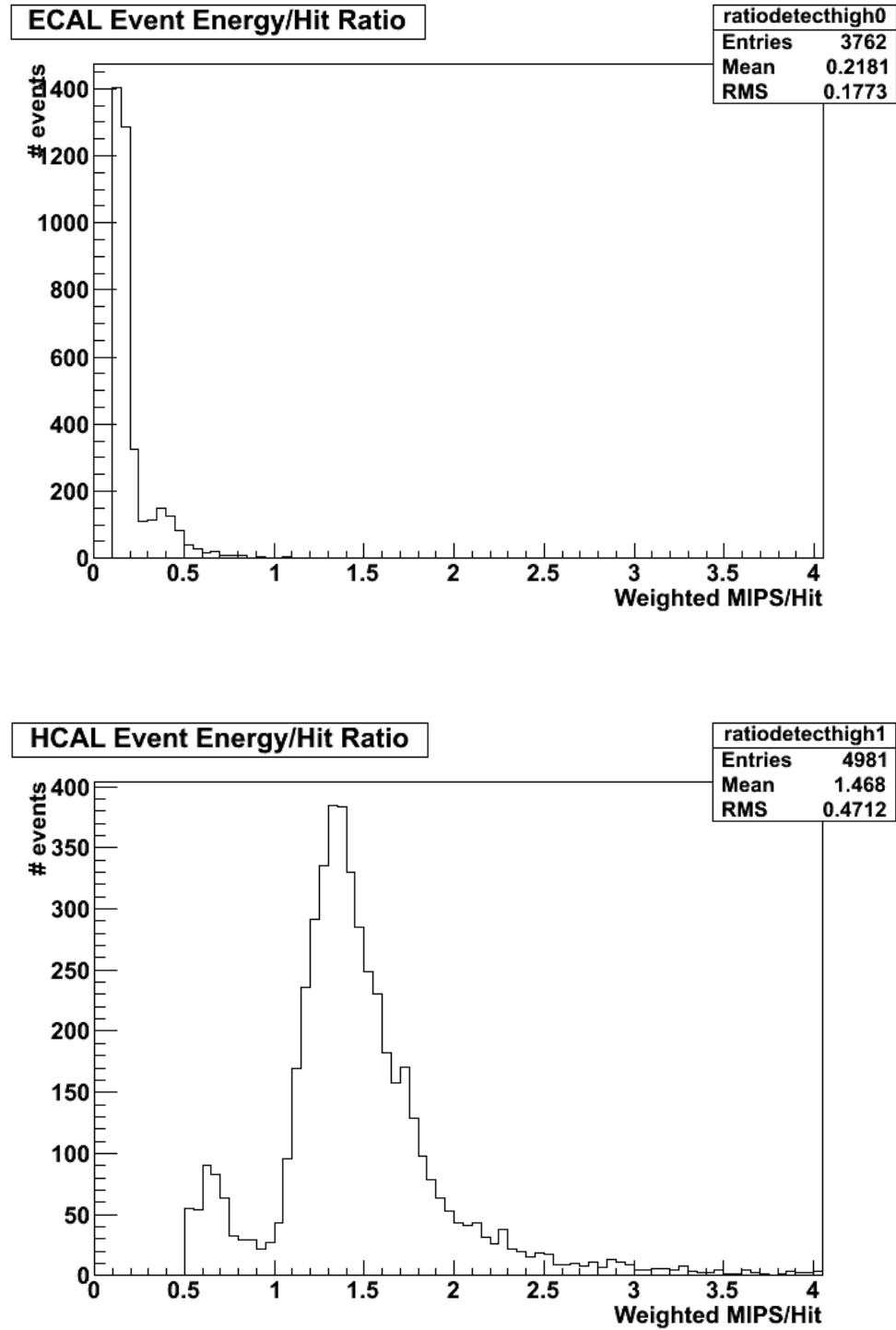


Figure 6.6: Energy to hit ratios from muon run in ECAL, HCAL and TCMT. (Continued on following page)

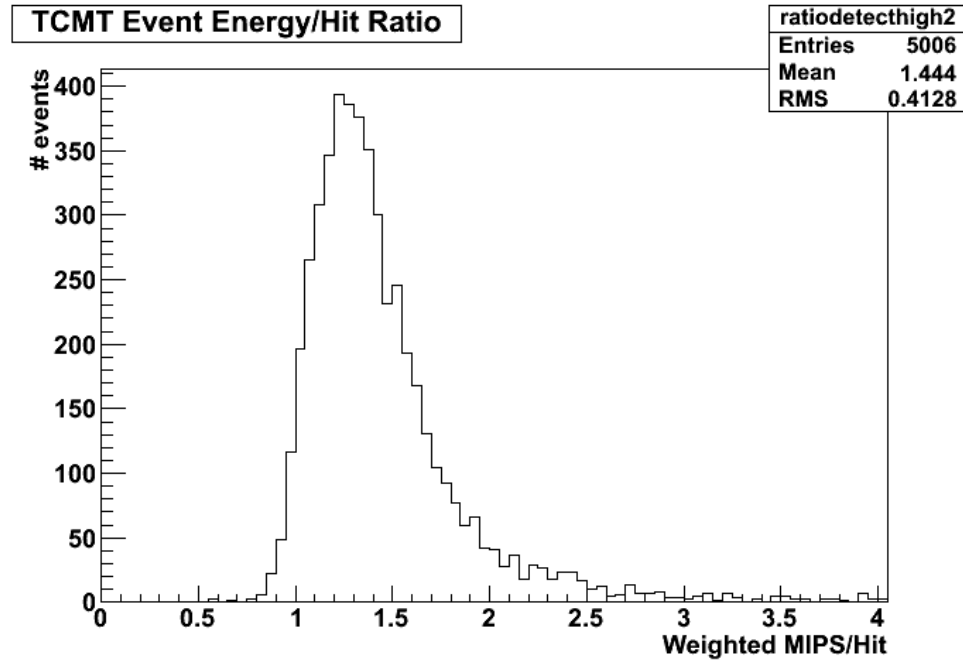


Figure 6.6: (Continued)

Table 6.2 Ratio Cut Efficiency

Detector	Muons Tagged	Detected by Ratio Cut	Efficiency
ECAL	2538	2520	99%
HCAL	2538	2415	95%
TCMT	2538	2434	96%
Complete Detector	2538	2305	91%

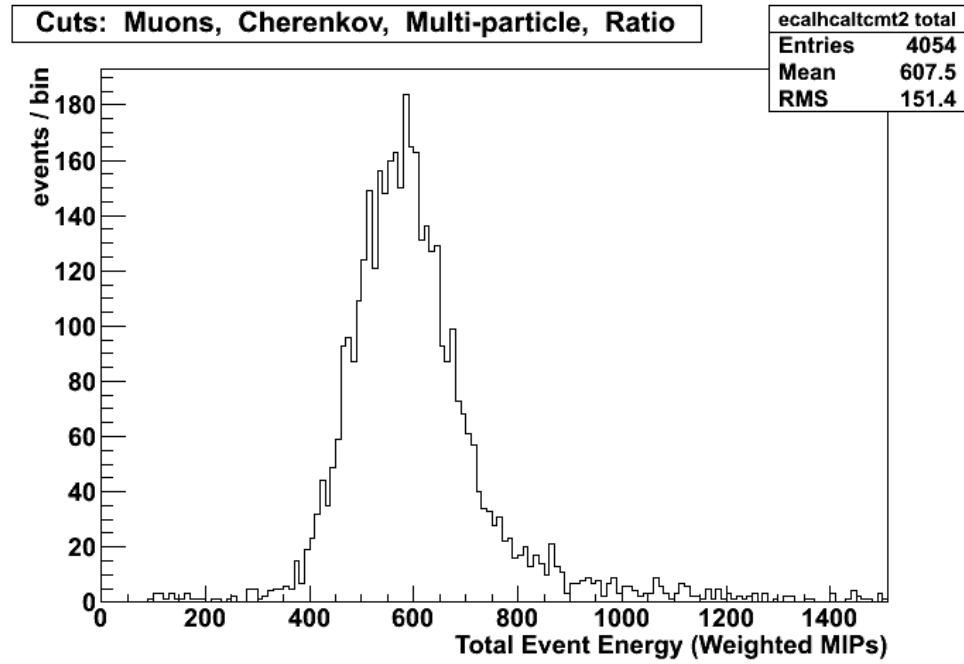


Figure 6.7: Energy spectrum with energy to hit ratio, muon veto, electron and double particle cuts applied.

Table 6.3 shows a breakdown of event types for a typical 20 GeV negative pion run. Of the events, 17.7% are contamination from multi-particles, muons, and electrons detected by the in-beam vetoes. Another one percent are muons rejected using the ratio cut derived from tagged muon profiles in muon runs. The remaining 81% events are used for analysis.

Table 6.3. Breakdown of Event Types

type of event	% events
multi-particles	9.5
electrons	5.6
muons(detected in 1m x 1m counter)	2.6
Probable untagged muon events	1.2
Analyzed events	81.1

CHAPTER 7

DETERMINATION OF SAMPLING WEIGHTS

As discussed in Chapter 5 sampling weights need to be determined to take into account the response of different components of the CALICE calorimeter system. If the calorimeter is hermetic, all of the energy of the event will be contained but the energy distribution between each of the components will be different from event to event. The method of using the slope of the inter-correlation plot as described in Chapter 5 requires some estimation and therefore is approximate. An alternative, more precise and rigorous method uses a least squares minimization technique to compute the weights.

The least squares method would require a minimization of the quantity:

$$S = \sum_{j=1}^N (E_0 - \sum_{i=1}^n A_i L_{ij})^2 \quad (7.1)$$

where n is the number of sections which could be individual layers or groups of layers, the A_i is the weight of the i^{th} section, and j runs over all events, N , and L_{ij} are the signals in the individual layers. E_0 is the beam energy.

There are three distinct sections of the ECAL, two distinct sections of the HCAL and two distinct sections of the TCMT with each characterized by different absorber thicknesses. Five to eight weights were used depending on the configuration used to

evaluate the performance of the TCMT. As an example, for a calorimeter which only includes three sections of the ECAL, corresponding to the three absorber thicknesses, and two sections of the HCAL, five weights are required. The first section of the HCAL includes the 18 fully instrumented layers. The second section corresponds to the 12 absorber layers in which every other layer was instrumented. As described in Chapters 9 and 10, 30 different configurations were studied based on the TCMT layers used. A set of weights for each configuration had to be generated. Configurations in which no magnetic coil was simulated had five to seven weights: five when only the ECAL and HCAL are used, six when the TCMT layers with thin absorber are added and seven when both thin and thick TCMT absorber sections are added.

For configurations in which a simulated coil was used, the layers of the TCMT included for post-coil sampling were treated as an additional section with its own weight. In the configurations with simulated coil six to eight weights were calculated: six when no layers of the TCMT were added to the HCAL and some of the thick absorber layers were used for post-coil sampling; seven when some of the thin TCMT layers were added to the ECAL and HCAL and some thick layers were used for post-coil sampling and eight when both thick and thin layers of the TCMT were added to the ECAL and HCAL and some thick layers used for post-coil sampling. All weighting was performed after the cuts described in Chapter 6 were applied.

The L_{ij} , from Equation 7.1 can be put into matrix form:

$$\mathbf{X} = \begin{bmatrix} L_{11} & \cdots & L_{1n} \\ \vdots & \ddots & \vdots \\ L_{n1} & \cdots & L_{nn} \end{bmatrix}$$

and the method of least squares minimization can then be used to minimize S for each weight:

$$\frac{dS}{dA_i} = 0$$

by applying:

$$C_n \mathbf{X}_{nm} = \mathbf{B}_n$$

where: n and m are the number of sections, C_n is a vector containing the weights and, \mathbf{B}_n equals the vector containing the energy collected by the calorimeter section. The matrix \mathbf{C} can then be determined by inverting \mathbf{X} and multiplying by \mathbf{B} :

$$C_n = \mathbf{X}_{mn}^{-1} \mathbf{B}_n$$

When using all layers of the TCMT for the analysis of energy resolution, two sections of the TCMT are used corresponding to the layers with fine and coarse absorbers. In this case there are seven sections to the detector system and therefore seven weights.

The implementation used to determine the weight based on the incident beam energy is:

$$C_i = \sum_{j=1}^N E_0 \mathbf{B}_j \mathbf{X}_{ij}^{-1}$$

where: C_i = weight for section i , N = number of sections, E_0 = the incident energy (20 for 20 GeV), \mathbf{B}_j is the mean energy per event collected in section i MIPs, and \mathbf{X}_{ji}^{-1} is the inverted matrix where \mathbf{X}_{ij} is event energy in section i times event energy in section j . The

weights are effectively conversion factors of GeV/MIP. The uncertainty is a function of the uncertainty in the beam energy which is on the order of 2% and the uncertainty in the mean MIPs per event which depends on the number of samples used in the calculation, which in this case is 5000 samples. The uncertainties add in quadrature and are in the range of one to two percent.

Table 7.1 shows the weights derived from a 20 GeV negative pion run for the 17 configurations in which successively more TCMT layers are added to the calorimeter system. Configuration 1 has no TCMT layers and Configuration 17 has all cassettes added. Columns ECAL1, ECAL2, and ECAL3 represent the weights for the three ECAL sections differing by absorber thickness. HCAL 1 represents the first 17 layers of the HCAL in which an active layer was placed between each absorber. HCAL 2 represents the section of the HCAL in which active layers were installed between every other absorber. The TCMT column labeled “Thin” represents the weight for the eight TCMT layers with a 1.9 cm absorber behind it. The TCMT “Thick” column represents the weight for the eight TCMT layers with a 10.2 cm absorber. The ECAL sections do not vary much between configurations. This is because most of the pions pass through the ECAL with little interaction. Fluctuations in energy deposition are not seen until a particle creates showers in the HCAL or TCMT. The greatest variation between configurations is seen in the thick TCMT section weights. This is expected as the absorber thickness varies greatly in this region relative to other regions.

Table 7.2 shows that weights used for studies with a coil simulated by skipping layers. The TCMT post-coil column holds the weights of the TCMT thick layers that

follow the simulated coil. The TCMT Thick XCAL column contains a weight for an active layer with a thick absorber layer if that layer is being added to the calorimeter system.

Table 7.1: Intercalibration Weights with Layers of the TCMT Added to the Calorimeter System Derived from a 20 GeV Negative Pion Sample.

no coil Config.	ECAL 1	ECAL 2	ECAL 3	HCAL 1	HCAL 2	TCMT Thin XCAL	TCMT Thick XCAL	TCMT post- coil
1	0.0087	0.0092	0.0135	0.0341	0.0871	0.0000	0.0000	-
2	0.0086	0.0092	0.0133	0.0339	0.0696	0.1737	0.0000	-
3	0.0086	0.0092	0.0133	0.0339	0.0664	0.1178	0.0000	-
4	0.0086	0.0092	0.0133	0.0339	0.0650	0.0879	0.0000	-
5	0.0085	0.0092	0.0133	0.0338	0.0643	0.0771	0.0000	-
6	0.0085	0.0092	0.0133	0.0337	0.0640	0.0677	0.0000	-
7	0.0085	0.0092	0.0133	0.0337	0.0638	0.0615	0.0000	-
8	0.0085	0.0092	0.0133	0.0336	0.0639	0.0567	0.0000	-
9	0.0085	0.0092	0.0133	0.0336	0.0638	0.0531	0.0000	-
10	0.0085	0.0092	0.0133	0.0335	0.0641	0.0453	0.0926	-
11	0.0084	0.0092	0.0133	0.0334	0.0639	0.0418	0.0984	-
12	0.0084	0.0092	0.0133	0.0333	0.0637	0.0402	0.0988	-
13	0.0084	0.0092	0.0133	0.0333	0.0635	0.0396	0.0968	-
14	0.0084	0.0092	0.0133	0.0333	0.0635	0.0391	0.0955	-
15	0.0084	0.0092	0.0133	0.0332	0.0633	0.0390	0.0944	-
16	0.0084	0.0091	0.0133	0.0332	0.0633	0.0388	0.0942	-
17	0.0084	0.0091	0.0132	0.0332	0.0632	0.0387	0.0940	-

Table 7.2: Intercalibration Weights with Layers of the TCMT Added to the Calorimeter System and Used to Simulate a Magnetic Coil and for Post-coil Sampling from a 20 GeV Negative Pion Sample.

coil Config.	ECAL 1	ECAL 2	ECAL 3	HCAL 1	HCAL 2	TCMT Thin XCAL	TCMT Thick XCAL	TCMT post- coil
1	0.0085	0.0091	0.0132	0.0335	0.0821	0.0000	0.0000	0.2084
2	0.0085	0.0091	0.0131	0.0334	0.0671	0.1553	0.0000	0.1839
3	0.0084	0.0091	0.0131	0.0334	0.0642	0.1075	0.0000	0.2581
4	0.0084	0.0091	0.0131	0.0334	0.0632	0.0801	0.0000	0.2474
5	0.0084	0.0091	0.0131	0.0334	0.0625	0.0707	0.0000	0.2396
6	0.0084	0.0091	0.0131	0.0333	0.0624	0.0623	0.0000	0.2300
7	0.0084	0.0091	0.0131	0.0333	0.0623	0.0566	0.0000	0.2233
8	0.0084	0.0091	0.0131	0.0332	0.0626	0.0533	0.0000	0.2805
9	0.0084	0.0091	0.0131	0.0332	0.0625	0.0500	0.0000	0.2737
10	0.0084	0.0091	0.0131	0.0332	0.0629	0.0429	0.0835	0.2618
11	0.0084	0.0091	0.0132	0.0331	0.0626	0.0409	0.0918	0.3411
12	0.0084	0.0091	0.0132	0.0331	0.0628	0.0396	0.0955	0.4174
13	0.0084	0.0091	0.0132	0.0333	0.0629	0.0397	0.0956	0.6190

CHAPTER 8

DETERMINATION OF THE SiPM SATURATION CORRECTION

The SiPM used in the TCMT is a multi-pixel avalanche photodiode operating in Geiger mode. An example of the design is shown in Fig. 8.1[32]. Fig 8.2[33] is a photograph of a SiPM and Fig. 8.3[34] is an enlargement showing the individual pixels. Each pixel is sensitive to a single photon. The SiPM output is the sum of the outputs of individual pixels. The ideal SiPM would be linear so that N photons will hit N pixels creating a signal N times that of a single photon. A real SiPM, however, has a finite number of pixels (in the case of the TCMT each SiPM has 1156 pixels) and behaves non-linearly. If two or more photons hit the same pixel, for example, the output will be equivalent to that of one photon. There is also a recovery time of several tens of nanoseconds in which a pixel cannot re-fire. Any other photons hitting the pixel during that time will have no effect. An algorithm that corrects for these effects must be developed to compensate for saturation in beam run data.

Figure 8.4 shows the response curve of a typical SiPM (device number 06799) from data taken at the Institute for Theoretical and Experimental Physics, Moscow (ITEP) (black squares). In comparison, the expected response if the device was linear is also plotted (blue triangles). Table 8.1 shows the response numerically. The twenty rows correspond to twenty levels of illumination. The “Illumination Level” column is the light

level used to illuminate the SiPM. The second column, “Pixels Activated,” gives the number of pixels activated at that illumination level; this is a measured value. The “Pixels Expected” column gives the number of fired pixels expected if the device was linear. The pixel response of 14.02 for a relative illumination level of 0.95 is used as the pixel/MIP value for the device. The “Correction Factor” column is the ratio of the “Pixels Expected” to “Pixels Activated” columns. The difference between the actual pixels fired to pixels expected can be up to three times when the device is fully saturated. However, up to an illumination level of 5.09 or approximately 86 pixels activated, the device is close to linear with correction factors to within one percent.

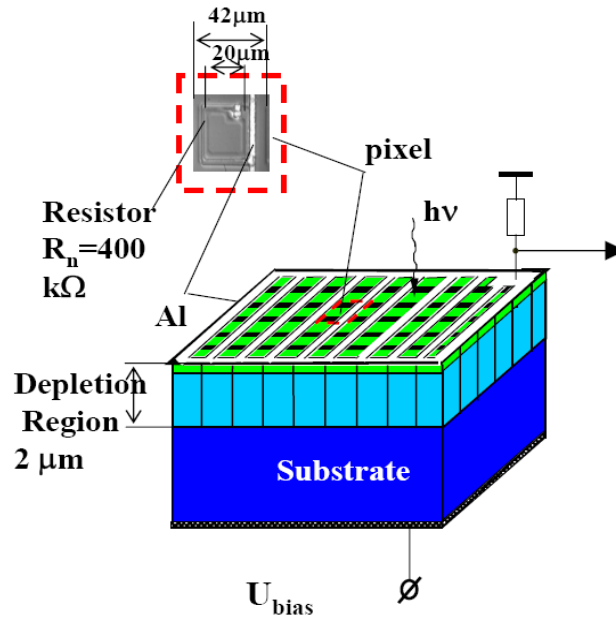


Figure 8.1: Diagram of silicon photomultiplier (SiPM) structure.

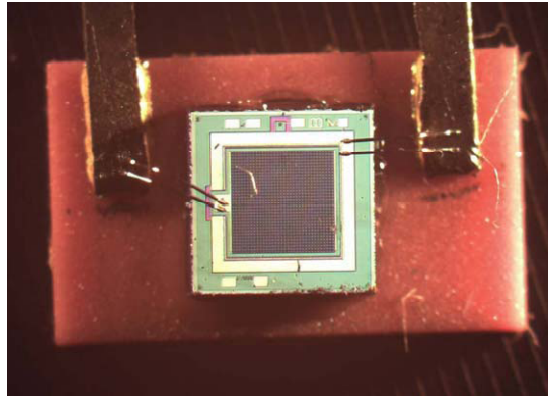


Figure 8.2: Photo of SiPM. (Gray center of photo-detector is approximately 1mm square).

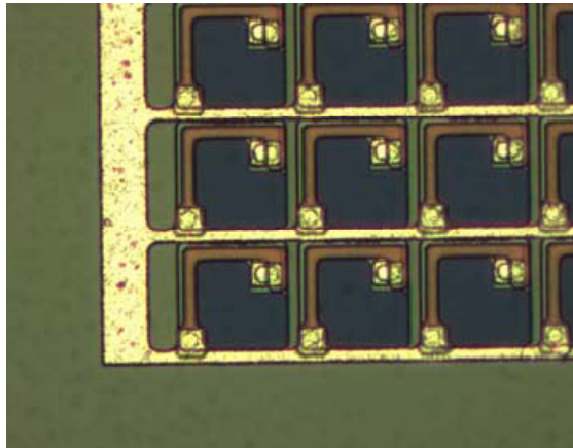


Figure 8.3: Detail of SiPM pixel structure. (Each pixel is approximately $25\text{ }\mu\text{m}$ square).

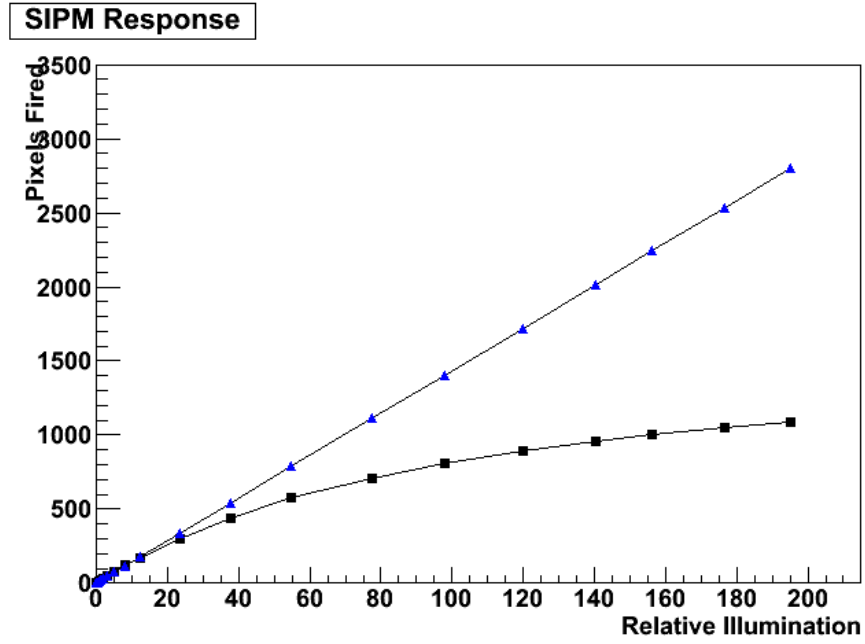


Figure 8.4: Measured response of a typical SiPM (black) and expected response if the device were linear (blue).

A response function can be approximated as:

$$N_{\text{pixels}} = N_{\text{tot}} [1 - \exp(-N_{\text{pe}} / N_{\text{tot}})].$$

In general, and more practically, an algorithm that uses linear interpolation can be used:

$$P_{\text{corrected}} = P_{\text{raw}} \left(S_n + \frac{(P_{\text{raw}} - P_n)(S_{n+1} - S_n)}{P_{n+1} - P_n} \right),$$

where P_{raw} is the number of pixels before correction, $P_{\text{corrected}}$ is the number of pixels after correction, P_n is the number of expected pixels in the lowest point in the interpolation interval, P_{n+1} is the number of pixels at the highest point of the interpolation interval, S_n is the calculated scaling factor the lowest point in the interpolation interval, and S_{n+1} is the calculated scaling factor at the highest point in the interpolation interval.

Table 8.1. Response of a Sample SiPM

Illumination Level	Pixels Activated	Pixels Expected	Correction Factor
0.00	0.00	0.00	0.00
0.43	6.32	6.35	1.00
0.70	10.09	10.33	1.02
0.95	14.02	14.02	1.00
1.42	21.23	20.96	0.99
2.31	34.34	34.10	0.99
3.77	55.91	55.65	1.00
5.90	86.03	87.08	1.01
9.32	132.57	137.56	1.04
13.77	190.24	203.25	1.07
26.07	326.98	384.79	1.18
41.95	470.14	619.18	1.32
60.43	603.65	891.95	1.48
85.34	743.15	1259.62	1.69
108.07	840.86	1595.11	1.90
132.35	924.66	1953.49	2.11
156.51	990.63	2310.09	2.33
175.63	1033.31	2592.30	2.51
200.52	1079.14	2959.68	2.74
223.93	1115.01	3305.21	2.96

Each SiPM has its own set of 20 scaling factors calculated from the raw pixel and relative illumination levels as measured at ITEP. Every hit used in this analysis is stored in terms of MIPs (see Chapter 5). To convert from MIPs to raw pixels the following formula is used: $P_{\text{raw}} = L_{\text{yield}} H_{\text{MIP}}$, where P_{raw} is the signal in uncorrected pixels fired, L_{yield} is the light yield in photo-electrons per MIP (PE/MIP), and H_{MIP} is the hit signal in MIPs. In the linear range the number of pixels fired is equal to the number of photo-electrons.

As can be seen in Table 8.1 the example SiPM is linear to within 2% up to 86 pixels. All SiPMs show similar behavior. Throughout this range the device can be treated

as linear. The interpolation scaling factors were generated from the ratio of expected to measured pixels fired. The “Pixels Expected” column was derived from a linearity constant calculated from the ratio of the pixels fired to relative illumination level of the first non-zero measurement point. The first measurement point is not necessarily the best point to derive the linearity constant. Other alternatives would be to take an average of the points in the linear range, to calculate the slope of the points in the linear range, or to take the maximum ratio found in the linear range and to use a scaling value of one for all points below the maximum in the linear range.

Several methods for deriving the linearization factor were evaluated. Method 1 used the first non-zero measurement point to derive the scaling factor for the entire series. This method can be seen in column 4 of Table 8.1. Table 8.2 is a comparison of three alternative methods. Column 1 is the number of raw pixels fired. Column 2 (Method 2) uses a linearity constant calculated from a fit of point two through five. Column 3 (Method 3) uses the highest linearity constant calculated from the first seven points. Column 4 (Method 4) uses the same constant as column three but forces all the lower points to 1.00. Methods 3 and 4 are the most different in the linear range.

To determine which of these methods is more satisfactory intercalibration weights were calculated for each and the final energy resolution and linearity of the full calorimeter compared.

Figure 8.5 plots the energy resolution of the complete calorimeter as a function of beam energy. Details on the determination of response are given in Chapter 9. Both methods have been plotted but they are within one percent and cannot be seen as separate

Table 8.2: Alternative Methods of Calculating Interpolated Scaling Factors

	Method 2	Method 3	Method 4
Raw Pixels Fired	Use linearity constant from fit of first 4 points	Use linearity constant from maximum ratio	Use linearity constant from maximum ratio and use 1.00 for all lower points
0.00	1.00	1.02	1.00
6.32	1.00	1.02	1.00
10.09	1.02	1.04	1.00
14.02	0.99	1.01	1.00
21.23	0.99	1.00	1.00
34.34	0.99	1.01	1.01
55.91	0.99	1.01	1.01
86.03	1.00	1.03	1.03
132.57	1.03	1.05	1.05
190.24	1.06	1.08	1.08
326.98	1.17	1.19	1.19
470.14	1.31	1.33	1.33
603.65	1.47	1.50	1.50
743.15	1.69	1.72	1.72
840.86	1.89	1.92	1.92
924.66	2.10	2.14	2.14
990.63	2.32	2.36	2.36
1033.31	2.50	2.54	2.54
1079.14	2.73	2.78	2.78
1115.01	2.95	3.00	3.00

points. Fig. 8.6 is a plot of the linearity of response and also shows that the methods are nearly indistinguishable. Since neither method can be shown to improve the resolution the fourth method has been chosen for all further analysis because the interpolation values are the same throughout the linear range.

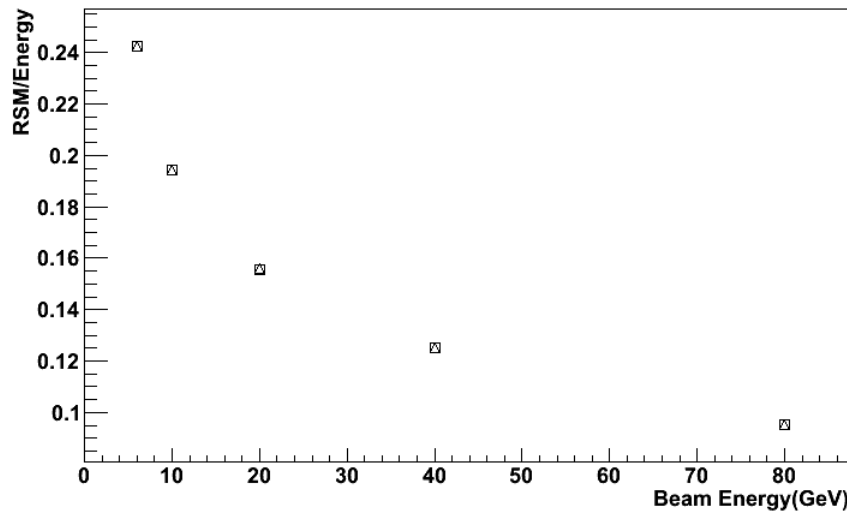


Figure 8.5: Plot of energy resolution to compare Method 3 and Method 4 for the calculation of interpolation scaling factors.

Although important for very energetic hits, on an event by event basis the saturation correction is not large. Fig. 8.7 is a plot of the hit energy spectrum for a 20 GeV pion run. All hits are less than 20 MIPs, and 88% of the hits have energy less than five MIPs. From Chapter 5, the average light yield is approximately 5.6 photons/MIP. Multiplying the MIPs by the light yield gives a maximum of 112 PE or pixels. These few very high MIP hits are only corrected by approximately 5%. Fig. 8.8 shows a comparison of the event energy spectrum for a 20 GeV pion sample containing the total energy of all

the TCMT strips in the event. The uncorrected event energy is plotted in red, the corrected is plotted in blue. There are only modest adjustments to the total event energy.

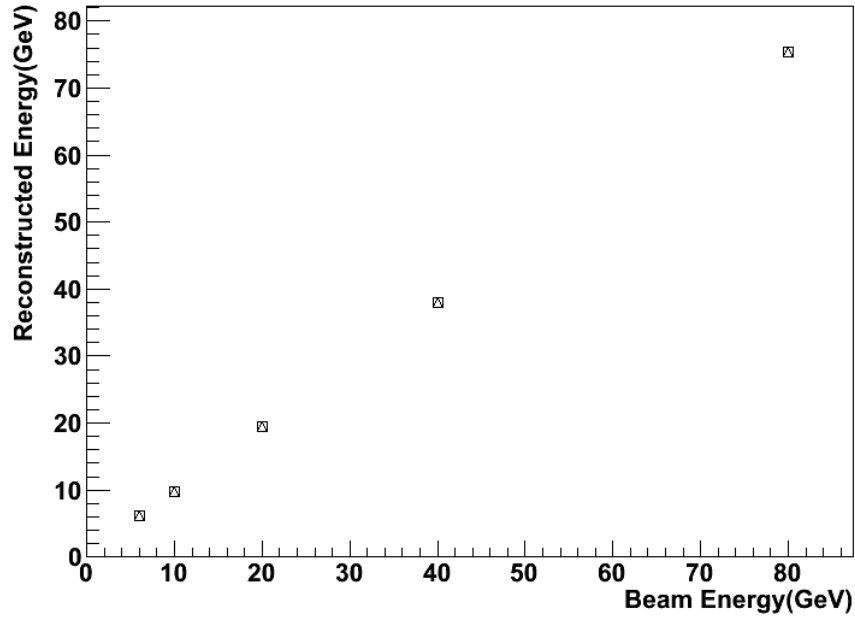


Figure 8.6: Plot of linearity to compare Method 3 and Method 4 for the calculation of interpolation scaling factors.

Figure 8.9 shows the uncorrected average response of 320 strips in the TCMT. There are 16 peaks each about six strips wide. These are strips in the center of the cassettes where the beam is concentrated. Only these central strips would have a significant contribution to the corrected energy. The other off-center strips have an average response of 2 MIPS. Unless the uncorrected response is over 4 MIPS the correction algorithm will not change the value significantly. (Note: there are a few strips with zero response. These strips are inactive usually due to a faulty SiPM sensor.) Fig. 8.10 shows the uncorrected maximum response for the 320 strips.

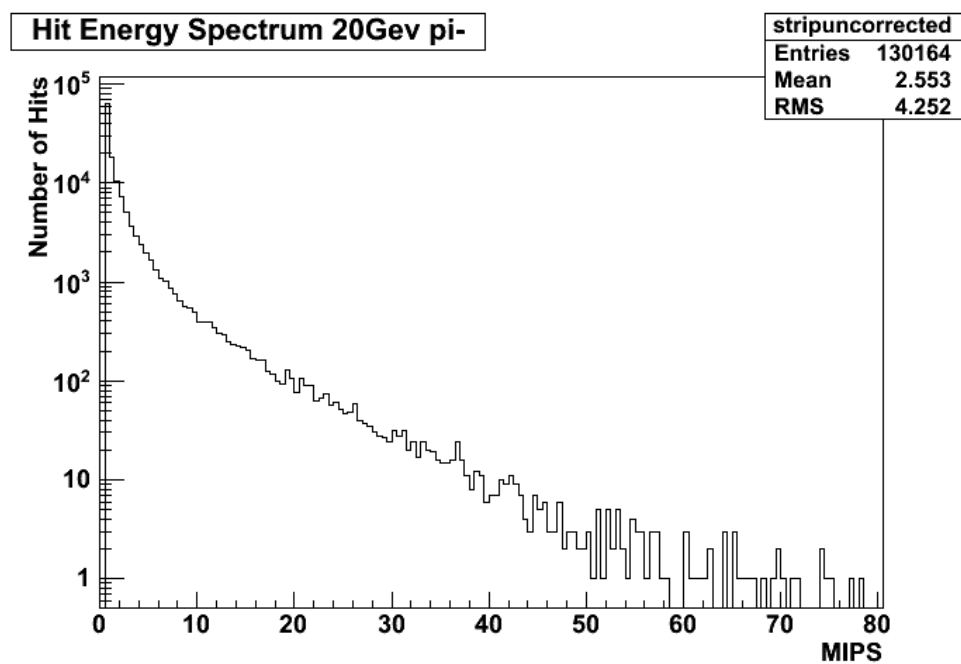


Fig 8.7: Hit energy spectrum for a 20 GeV pion run.

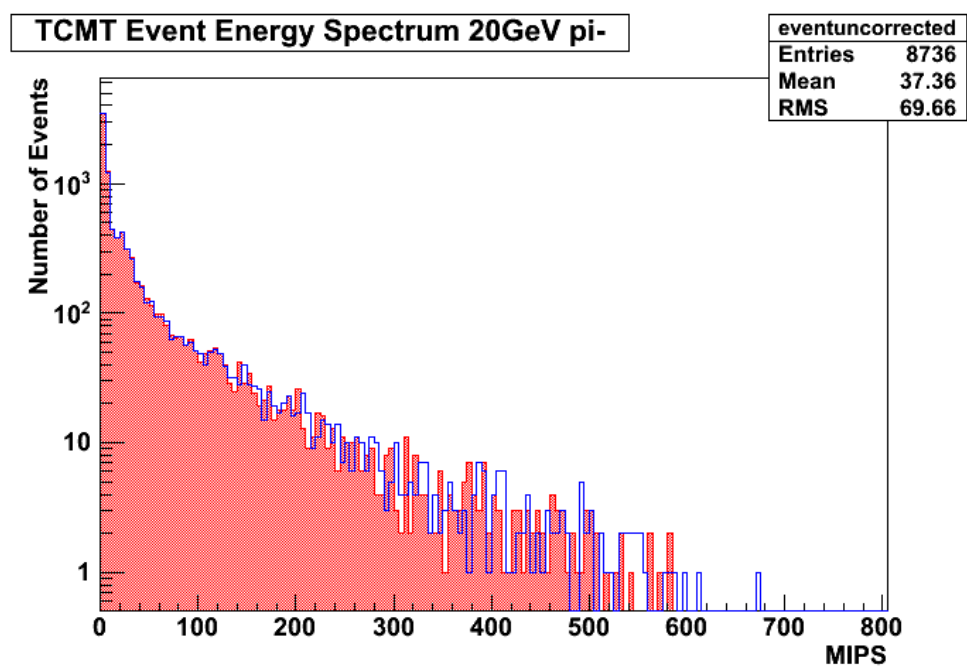


Figure 8.8: Corrected versus uncorrected event energy.

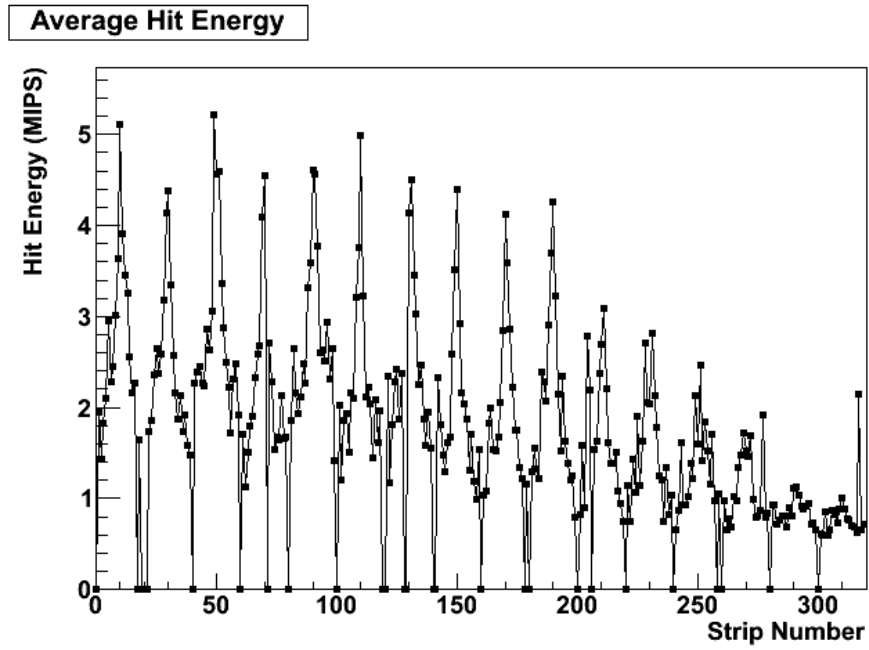


Figure 8.9: Average response of all strips for a 20 GeV pion run.

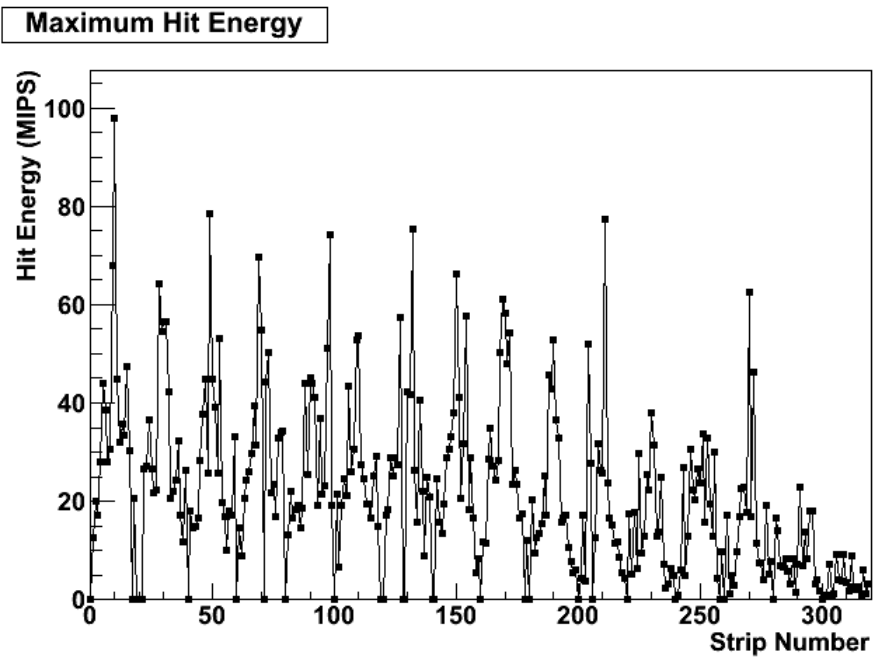


Figure 8.10: Maximum response of all strips for a 20 GeV pion run.

Figure 8.11 shows the increase in MIPS due to the saturation correction for hits. The number of hits outside of the linear range is 1582. With the number of hits in this sample equal to 59389 only 2.7% of the hits are corrected. For 10 GeV pions 1.2% of the hits were outside of the linear range and for 80 GeV pions 5.8% were outside of the range. The increase in average event energy can be seen in Fig. 8.12.

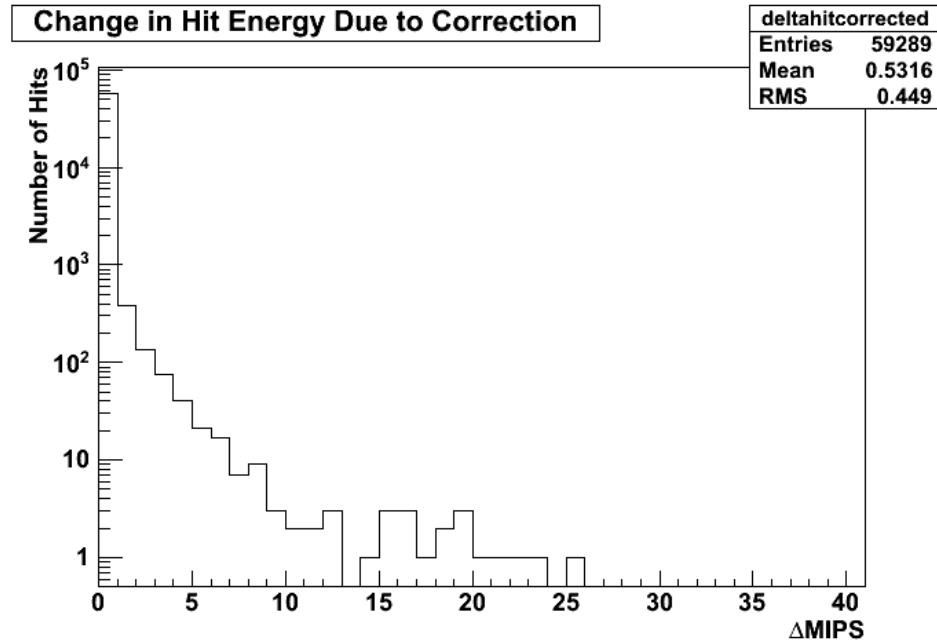


Figure 8.11: Increase in energy in MIPS due to saturation correction algorithm for individual hits.

Figure 8.13 shows the corrected to uncorrected ratio for event totals in the TCMT. The mean of 1.013 indicates a very small contribution to the total energy due to saturation correction.

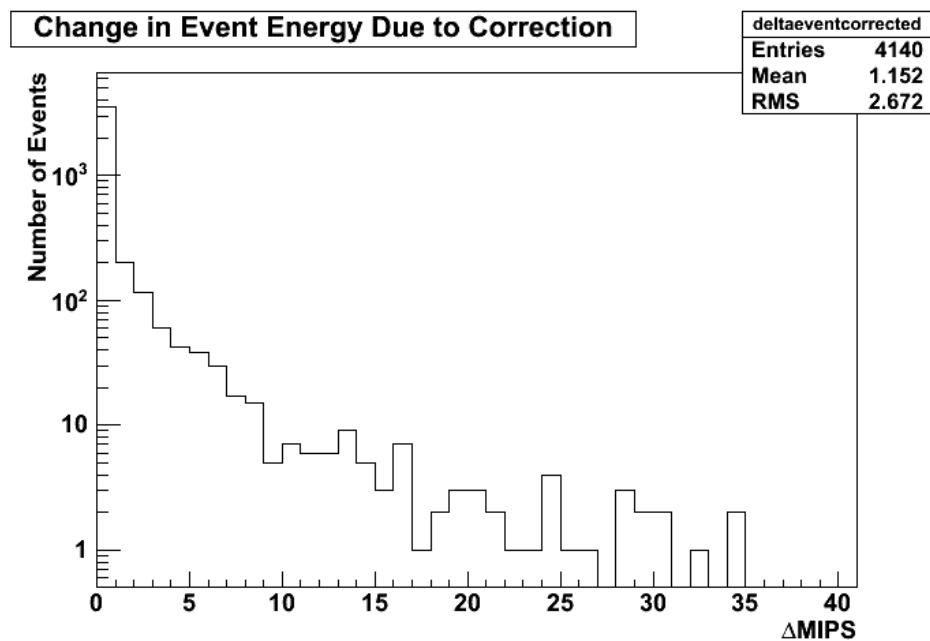


Figure 8.12: Increase in energy in MIPS due to saturation correction algorithm for event totals.

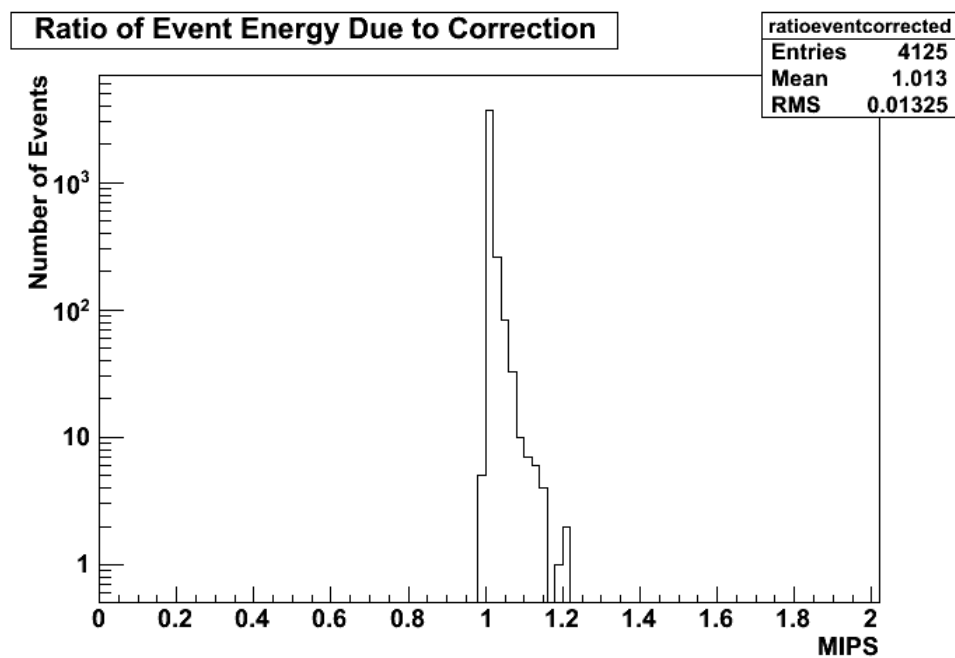


Figure 8.13: Ratio of saturation corrected to uncorrected event total energies in TCMT.

Figure 8.14 shows the ratio of saturation corrected energy to uncorrected energy for the event totals in the TCMT for a range of beam energies. The correction algorithm changes the energy by less than 3% over the beam energies studied. The higher the beam energy the more energy is deposited in the TCMT and the more significant the effect. Even at 80 GeV, the maximum tested in the 2006 run, the effect is just over 2%. Most hits are of low energy so the correction does not contribute much to the total corrected event energy. Therefore the precise algorithm for saturation correction has little impact on the overall performance.

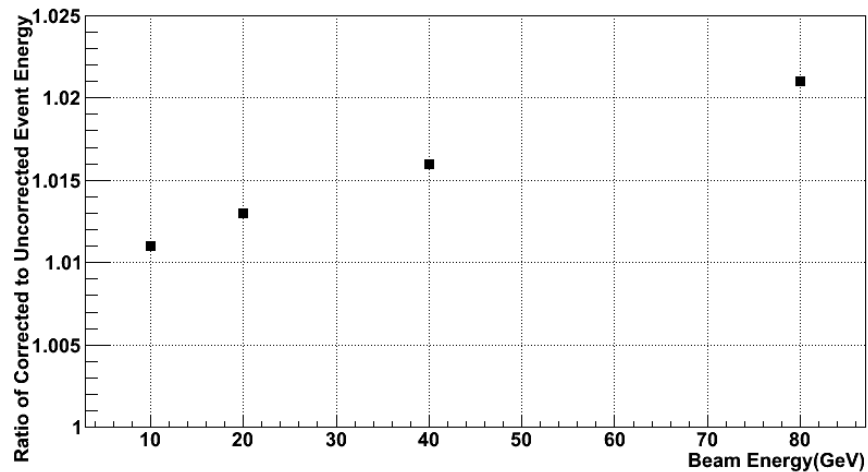


Figure 8.14: Ratio of event energy with and without saturation correction as a function of beam energy.

CHAPTER 9

RESOLUTION AND LINEARITY AS A FUNCTION OF CALORIMETER THICKNESS

9.1 Resolution as a Function of Calorimeter Thickness

A primary goal of the TCMT is the improvement of the full detector energy resolution. The energy resolution is typically taken to be the variance of a Gaussian fit to an energy distribution divided by the fit mean of the total energy.

$$E_{\text{res}} = \sigma/E_{\text{total}}.$$

In this study the mean and RMS are used in order to properly evaluate the tails.

$$E_{\text{res}} = \text{RMS}/E_{\text{total}}.$$

Studies of the mean energy and energy resolution were performed as a function of the number of TCMT layers used. Trailing layers were removed to study the effect on containment.

Figure 9.1 compares a 20 GeV negative pion energy spectrum of the CALICE detector without the TCMT (0 TCMT layers used, i.e. use only the ECAL and HCAL) compared to the spectrum with the TCMT (16 TCMT layers used which is the complete TCMT). The spectrum in Fig. 9.1 has been corrected for saturation and has the full set of quality and background requirements described in Chapter 6. In addition the weights

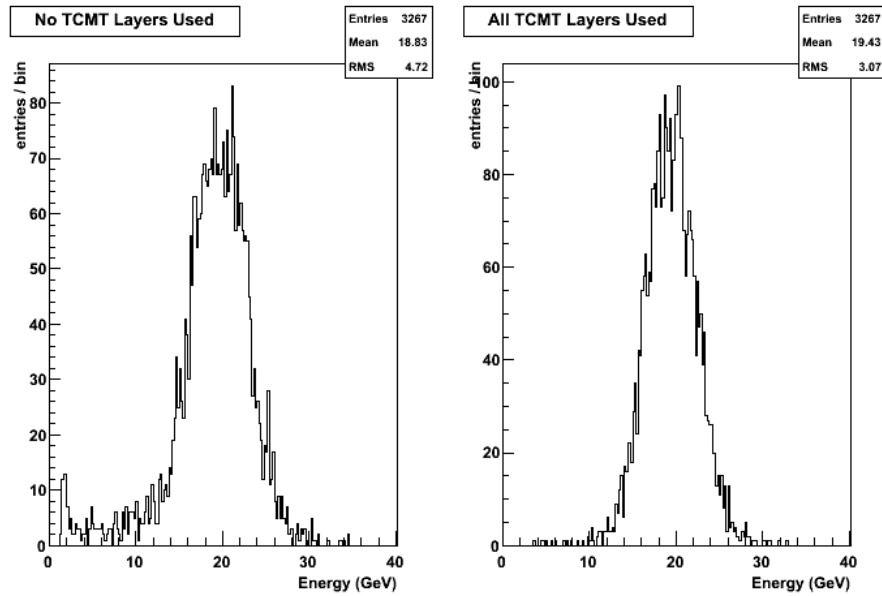


Figure 9.1: Comparison of the energy spectrum with and without full TCMT.

have been determined for each configuration as described in Chapter 7. (The weights were calculated after saturation correction). The low energy tail, consisting of genuine pion events that are not fully contained in the calorimeters, is significantly reduced with the addition of the full TCMT. Configurations using the partial TCMT have low energy tails intermediate between these two extremes. The mean shifts indicating a higher total energy collected and the variance decreases both corresponding to an improvement in energy resolution.

For this analysis the energy resolution is quantified with the metric of the ratio of the root-mean-squared (RMS) to the mean energy. The RMS typically gives a larger resolution than obtained from the variance of a Gaussian fit, and by definition is larger than that using the RMS-90 statistic. RMS-90 is the root-mean-squared deviation from

the mean in the smallest energy range containing 90% of the events. However, it is necessary to use the RMS/mean ratio to include the low energy tail of non-Gaussian energy distributions which arise due to energy leakage in configurations that do not use the full TCMT. The energy resolution of the full detector for a 20 GeV negative pion sample is found to be 0.157 ± 0.002 . In comparison, the energy resolution calculated using RMS-90 is 0.120 ± 0.002 .

Figure 9.2 shows the energy resolution as a function of the number of interaction lengths for 20 GeV pions. The energy resolution is calculated as:

$$\sigma_E = \text{RMS}/E_{\text{mean}}$$

The first point has no additional TCMT layers while the final point incorporates all sixteen layers. The energy resolution of the ECAL and HCAL alone is approximately 26%. The resolution improves to 17% when using 2.5 interactions lengths or eleven layers of the TCMT. The outermost five layers have diminishing impact.

9.2 Separation of Stochastic and Constant Components of Resolution

As described in Chapter 3 the energy resolution is traditionally given as a function of three terms:

$$\frac{\sigma(E)}{E} = \frac{N}{E} \oplus \frac{S}{\sqrt{E}} \oplus C$$

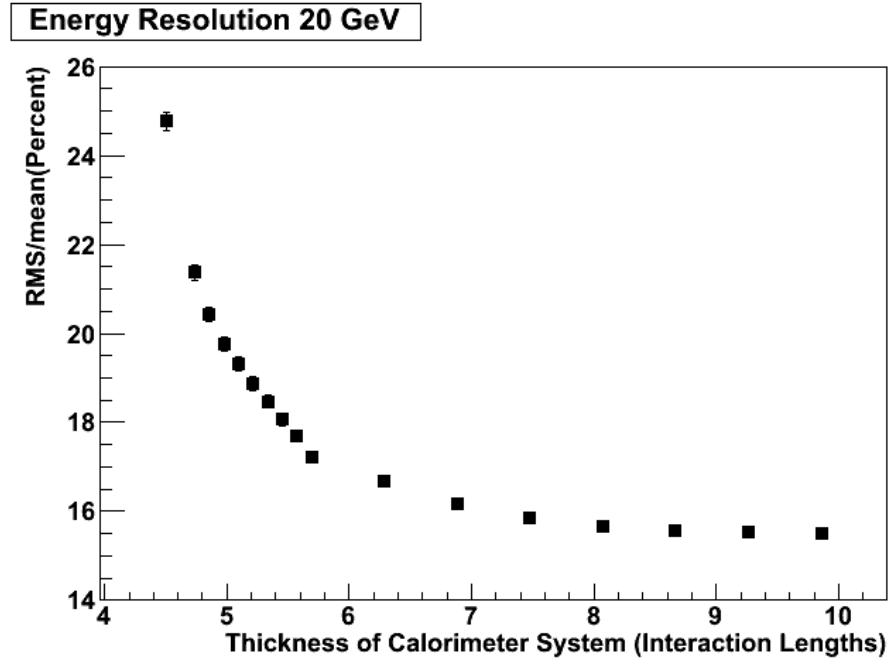


Figure 9.2: Energy resolution as a function of interaction lengths used in the TCMT.

where N is the noise term due mostly to electronic noise and has a lesser effect at higher energies; S is the stochastic term due to statistics-related fluctuations, shower fluctuations, PE statistics, dead material in front of calorimeter, and sampling fluctuations; and C is the constant term due to detector non-uniformity and calibration uncertainty. The variance is taken to be the square of the RMS of the energy spectra at the respective beam energies. The variance can be written as:

$$\sigma^2(E) = N^2 + S^2 E + C^2 E^2$$

Plotted in this way a fit can be made to find the constants: N , S , and C .

Figure 9.3 is a plot of the energy resolution as a function of energy for pions and inclusion of all 16 TCMT layers. Uncertainties in the data points are on the order of 1%.

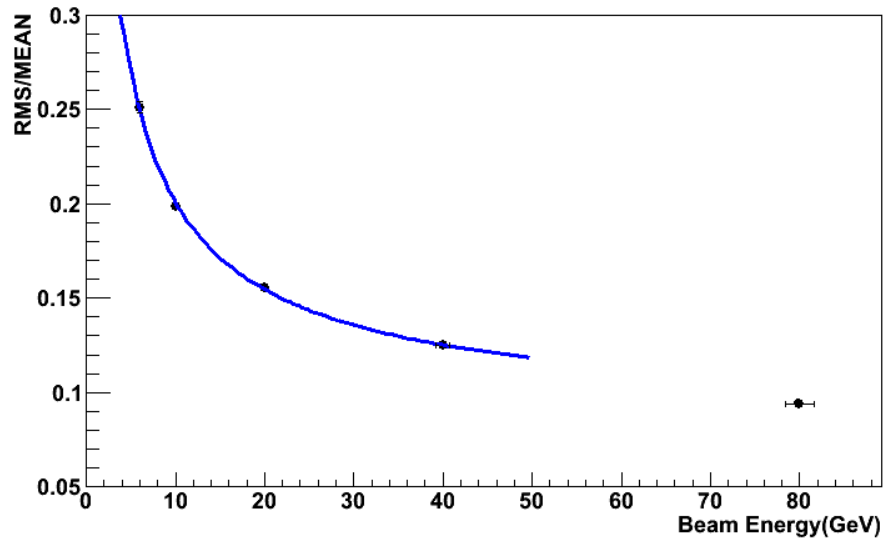


Figure 9.3: Energy resolution of the full calorimeter response to negative pions as a function of energy fit with a second-degree polynomial.

The curve represents the results of a second-degree polynomial fit. N is small. The final measurement is not included as the fit fails with a very high chi-squared if included. This effect was noted previously [35][36]. S is 0.573 ± 0.036 and C is 0.087 ± 0.016 .

9.3 Linearity

In Chapter 8, the linearity was used to assist with the evaluation of saturation correction algorithms. The residual is computed as:

$$Residual = 100 * (E_{Beam} - E_{reconstructed})/E_{Beam}$$

where: $E_{\text{reconstructed}}$ is the reconstructed energy and E_{beam} is the beam energy of a pion run. The weights used at all energies were determined from a 20 GeV pion sample. Figure 9.4 shows the linearity deviates by approximately 3% or less with the response fixed to 20 GeV for the 20 GeV pion sample.

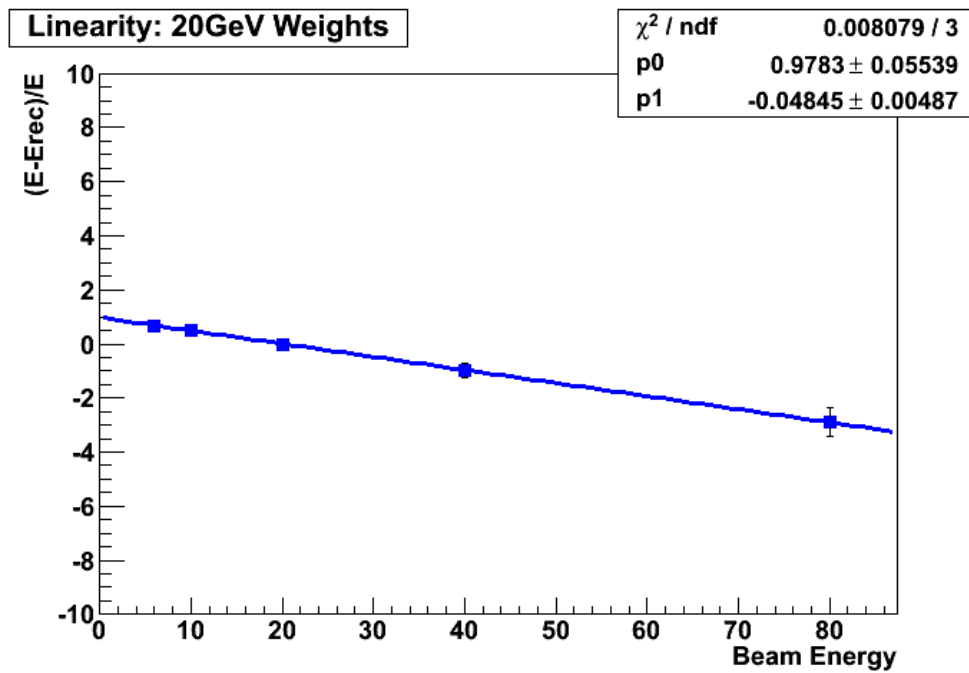


Figure 9.4: Linearity

9.4 Leakage

The TCMT can be used to measure the leakage from the calorimeter system. Using the October 2006 data the calorimeter system is defined to be the ECAL + HCAL + first seven layers of the TCMT for a total thickness of 5.44 interaction

lengths (close to the design thickness of the ECAL+HCAL of 5.5 interaction lengths in the 2007 runs). The remaining nine layers of the TCMT are used to calculate the leakage. The fractional RMS is the RMS of the distribution of the event energy of the calorimeter system divided by the selected beam energy in GeV. The leakage is calculated as:

$$L_{\text{event}} = (E_{\text{total}} - E_{\text{calorimeter}}) / E_{\text{total}},$$

where L_{event} = leakage for the event, $E_{\text{calorimeter}}$ = energy measured by the ECAL, HCAL and any layers of the TCMT used to supplement the HCAL, and E_{total} = energy measured by the total detector including the additional layers of the TCMT not included in $E_{\text{calorimeter}}$, for every event. The mean and RMS of all events are reported in Table 9.1 as "leakage." In summary the leakage is approximately 3% and 8% for 10 and 80 GeV pions.

Table 9.1: Leakage Measurements

	10 GeV	80 GeV
Fractional RMS	0.203+/-0.002	0.118 +/-0.001
Leakage (mean)	0.032 +/-0.082	0.076 +/-0.001
Leakage RMS	0.082 +/-0.001	0.117 +/-0.001
Fraction of events with leakage >= 10%	0.030 +/-0.000	0.061 +/-0.001

CHAPTER 10

COIL STUDIES

TCMT data, taken in October 2006, was used to study the impact on energy resolution of deepened calorimetry and calorimetric sampling after a magnetic coil. Most ILC detector designs include a calorimeter inside a magnetic coil with a depth of around five interaction lengths. By adding forward layers of the TCMT to the relatively thin hadronic calorimeter showers could be contained and the energy resolution improved. A final ILC configuration would typically include a magnetic coil of approximately two interaction lengths thick between the calorimeter and subsequent instrumentation. No coil was included in the CALICE prototype but the material of a coil can be simulated with forward absorber layers of the TCMT simply by removing these layers from analysis.

Sampling fractions are calculated using the least squares minimization technique described in Chapter 7 as shown in Table 7.4. The HCAL is taken to have a depth of 3.5 interaction lengths. The last two absorber layers of the HCAL were not instrumented during the October run and are treated as leading absorber layers for the additional layers in this study.

Table 10.1 describes the configuration of the TCMT layers used in the coil simulations. It is an abridged form of Table 3.1. The first column indicates the number of TCMT layers added to the ECAL and HCAL to extend the calorimeter forward of the

simulated coil. In terms of the TCMT layer number, the first column also identifies the first layer of the forward edge of the simulated magnetic coil. The second column identifies the first layer of the TCMT after the simulated coil. The third column indicates the total number of TCMT layers remaining to simulate the post-coil calorimetry.

The left panel of Fig. 10.1 shows an 80 GeV pion beam energy spectrum for the ECAL and HCAL with no layers of the TCMT added to the calorimeter system. The right panel of Fig. 10.1 shows the energy spectrum for a simulated coil immediately after the HCAL followed by sampling with the remaining layers of the TCMT. (This configuration corresponds to the first row of Table 10.1.) The left side tail is reduced by the post coil sampling leading to improved energy resolution.

10.1. TCMT Layers Used for Coil Simulation Analysis

Layers of TCMT added to calorimeter	End of Simulated coil/first layer	TCMT Layers Used for TCMT used behind coil
0	10	6
1	10	6
2	11	5
3	11	5
4	11	5
5	11	5
6	11	5
7	12	4
8	12	4
9	12	4
10	13	3
11	14	2
12	15	1

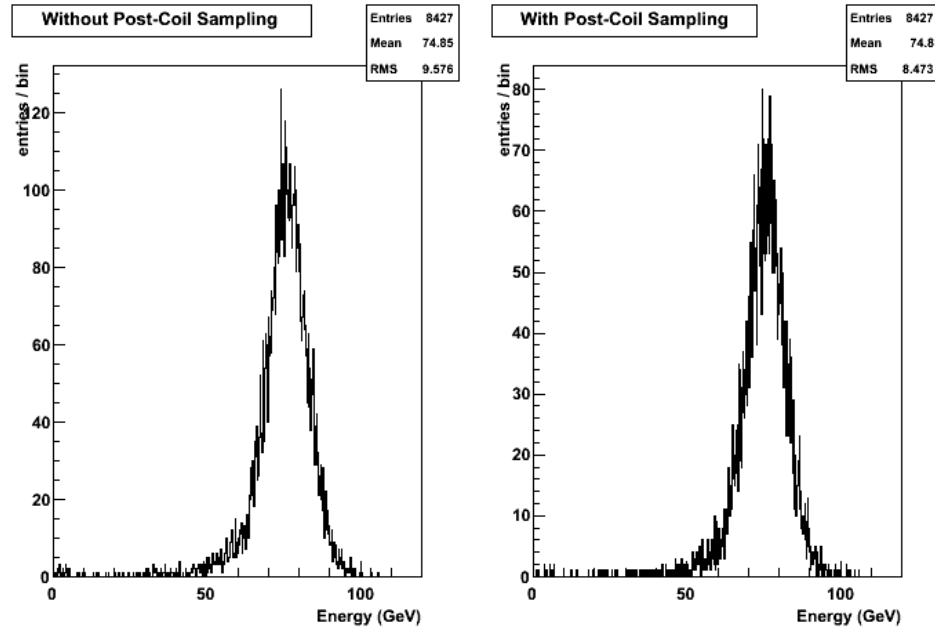


Figure 10.1: Energy spectra with zero layers of TCMT added to the calorimeter system (left) and with simulated coil and subsequent post-coil sampling (right) for an 80 GeV pion run.

Figure 10.2 plots the energy resolution of a 20 GeV negative pion sample for a calorimeter system incorporating the ECAL, the HCAL, and the first n forward layers of the TCMT (red or upper symbols) and the resolution for a system including the ECAL, the HCAL, n forward layers of TCMT, a 1.8λ coil gap, and the remaining layers of the TCMT (blue or lower symbols.) The energy resolution corresponds to the root-means-square of the energy distribution, illustrated with Fig. 10.1, divided by the average energy. The upper curve (red) shows that extension of the calorimeter from 4.5 to 7 interaction lengths dramatically improves resolution from 25.5% to 17.5%. The leftmost upper (red) point corresponds to no calorimeter extension and the leftmost lower (blue)

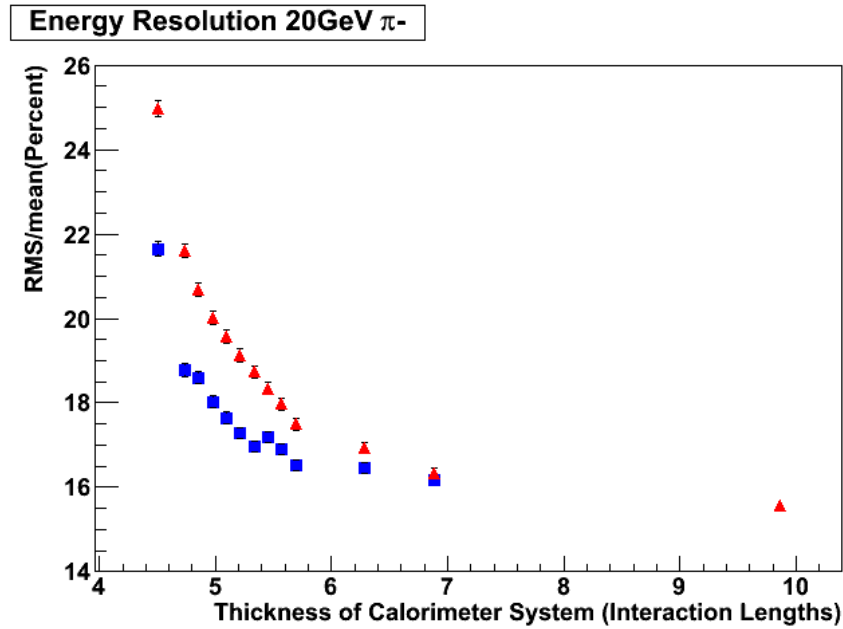


Figure 10.2: Comparison of the energy resolution of a 20 GeV negative pion sample with a simulated coil with (blue or lower points) and without (red or upper points) final TCMT layers after coil.

point to a coil immediately after the HCAL followed by additional sampling. Note the sampling improves resolution from 25.5% to 22.5%.

As shown in Fig. 10.2, at a depth of 5.5λ , a typical calorimeter depth for proposed ILC detectors, the additional sampling layers improve energy resolution for a 20 GeV pion by 2% which corresponds to a relative improvement of 11%. The rightmost points in Fig. 10.2 correspond to an HCAL extended by the full length of the TCMT and a coil with little or no additional sampling. The data indicate that for a coil beyond seven interaction lengths the post-coil sampling provides negligible improvement for a 20 GeV pion.

Figure 10.3 shows the performance of the simulated coil and TCMT system for 10, 20, 40, and 80 GeV beam energies as a function of calorimeter depth (inside the simulated coil.) Subsequent sampling after the simulated coil is included. The 4.5 interaction length thickness is the configuration in which the simulated coil begins immediately after the HCAL and no additional layers of the TCMT are added to the ECAL and HCAL before the coil. The 4.95 interaction length calorimeter includes two TCMT layers added to the calorimeter. The 5.5 interaction length point uses seven TCMT layers added to the calorimeter. The 6.9 interaction length configuration uses eleven TCMT layers added to the calorimeter and only two layers for post coil sampling. The resolution improvement increases with energy for all coil radii.

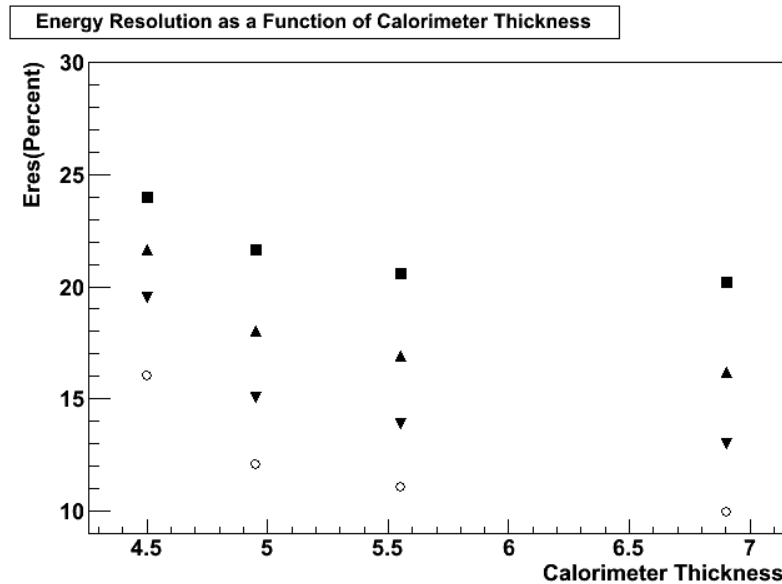


Figure 10.3: Resolution as a function of inner calorimeter depth inside the simulated coil and with subsequent sampling. Points are for 10 GeV (top), 20 GeV, 40 GeV, and 80 GeV (bottom) pions.

Figure 10.4 shows the energy resolution as a function of beam energy. The curves illustrate the resolution for different locations of the simulated coil. As noted earlier the resolution improves with beam energy. Moreover, as expected, the further the coil from the interaction region (or the deeper the inner calorimetry), the greater the improvement in energy resolution.

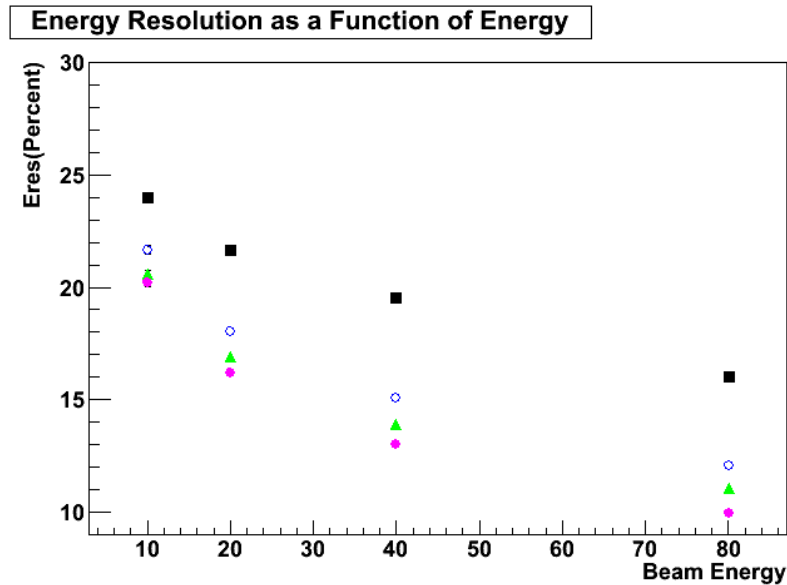


Figure 10.4: Resolution as a function of beam energy for four different coil depths with subsequent sampling (Solid squares (top)= 4.5λ , Open circles= 4.95λ , Solid triangles= 5.55λ , Solid circles (bottom)= 6.9λ .)

Figure 10.5 compares the energy resolution of a 5.5λ thick calorimeter with and without a coil plus post-coil sampling. The absolute resolution improves by 1% at all energies. Figure 10.6 shows the relative improvement of the energy resolution as a function of energy when a calorimeter is extended by a coil and subsequent sampling

layers. In this example the coil is at a depth of 5.6λ . At 20 GeV the TCMT improves resolution by 6%.

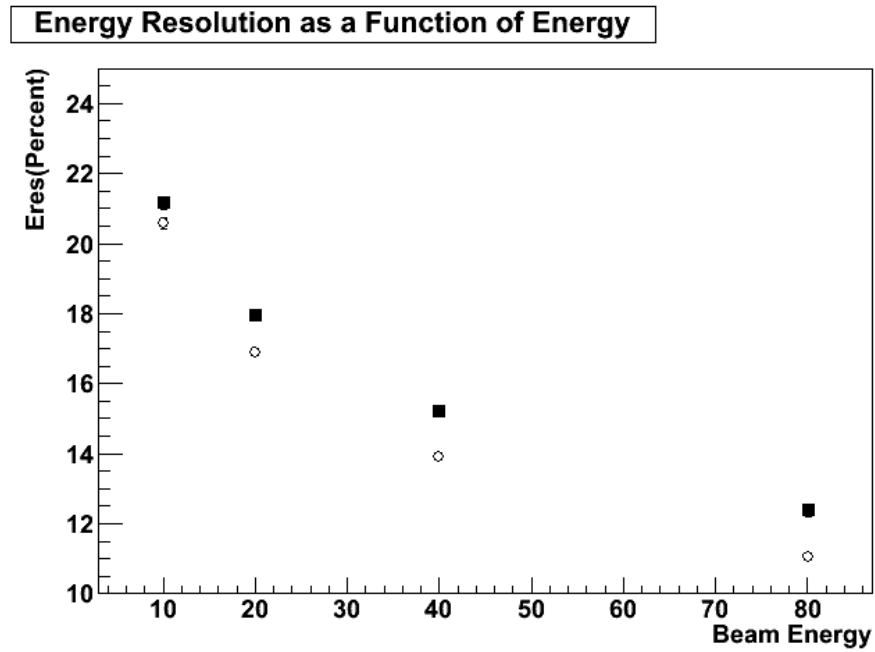


Figure 10.5: Energy resolution versus energy for a 5.5λ calorimeter system without a coil (solid squares) and followed by a simulated coil and post-coil sampling (open triangles).

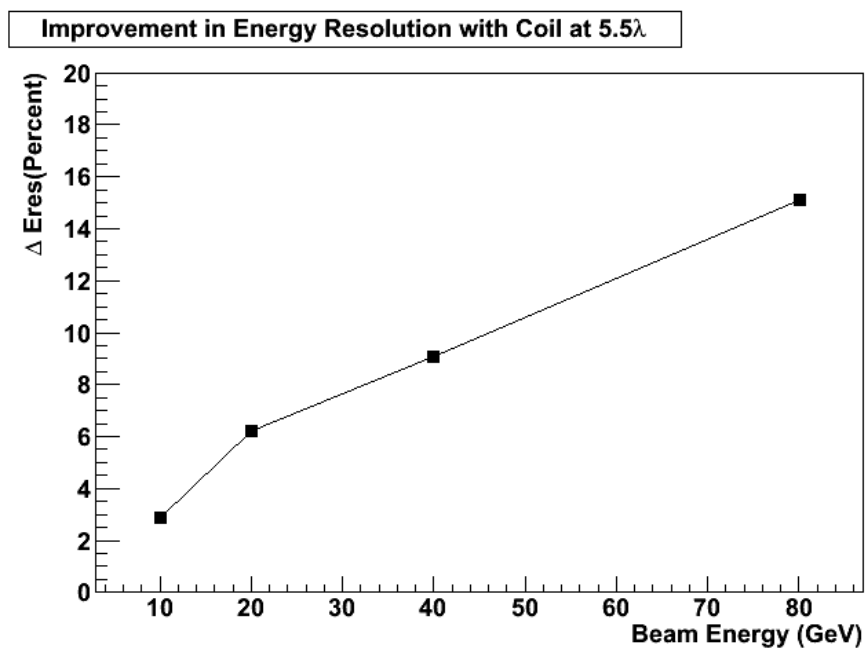


Figure 10.6: Relative change in resolution with and without coil and subsequent sampling.

CHAPTER 11

CONCLUSIONS

The proposed ILC requires a detector with superior jet energy resolution of $30\%/\sqrt{E}$ or better near the Z-pole region (91 GeV). To achieve this goal, prototypes for a high granularity detector designed to use Particle Flow Algorithms have been developed by the CALICE consortium. One major limitation on detector resolution is the depth of the hadron calorimeter contained within a magnetic coil. The HCAL thickness in ILC detector designs are approximately 5.5 nuclear interaction lengths in depth. This is too thin to contain the most energetic showers and late showering pions. To compensate for this deficiency, the CALICE Tail Catcher/Muon Tracker has been designed to extend the calorimetry as well as function as a muon tracking system. The prototype design also provided an opportunity to simulate the impact on energy resolution of a magnetic coil in various configurations and to study the use of silicon photomultipliers (SiPMs) in particle detectors.

This analysis shows that the TCMT contains leakage and improves energy resolution. The effect of the TCMT both with and without a coil is more significant as energy increases. Inclusion of all sixteen layers of the TCMT to the 3.5λ thick CALICE calorimeter in the October 2006 test beam configuration improves pion resolution by 9.3% at 20 GeV, a relative improvement of 37%, and 10.8% at 80 GeV, a relative

improvement of 55%. For calorimeter system depths that are under consideration for ILC detectors the addition of TCMT layers after a coil of 1.8λ improves energy resolution. For a coil situated outside a 5.5λ calorimeter system, a typical configuration for proposed ILC detectors, a TCMT would improve the absolute energy resolution of 20 GeV pions by 1%, a relative improvement of 6% and for 80 GeV pions by 2%, a relative improvement of 10%.

REFERENCES

- [1] <http://www-sldnt.slac.stanford.edu/alr/images/simplemodel2.gif>
- [2] Perkins, D., *Introduction to High Energy Physics* Cambridge: Cambridge University Press, pg. 267 (2000).
- [3] Alvarez-Gaume, L., et al. *Physics Letters B, Review of Particle Physics*. Amsterdam: Elsevier (2008).
- [4] Brient, J-C., Laboratoire Leprince-Ringuet, “PFA AND TEST BEAM” LLR – Ecole polytechnique,
<http://indico.fnal.gov/getFile.py/access?contribId=33&sessionId=17&resId=0&materialId=slides&confId=441> (2007).
- [5] Thomson, M., Detectors for a Future Lepton Collider Lecture 3: Calorimetry,
http://www.hep.phy.cam.ac.uk/~thomson/talks/CERN_Academic_Training_Lecture_III_Final.pdf (2010).
- [6] Greene, D., Jet Energy Resolution Due to Calorimetric Resolution,
<http://lss.fnal.gov/archive/test-fn/0000/fermilab-fn-0652.pdf> (1997).
- [7] <https://twiki.cern.ch/twiki/bin/view/CALICE/WebHome>
- [8] http://physics.bu.edu/NEPPSR/2007/TALKS-2007/NEPPSR_Butler_2007.pdf (2007).
- [9] Fernow, R., *Introduction to Experimental Particle Physics*. Cambridge: Cambridge University Press, pg. 271 (1986).
- [10] Wigmans, R., *Calorimetry: Energy Measurements in Particle Physics*. Oxford: Clarendon Press, pg. 78 (2000).
- [11] <http://silicondetector.org/display/SiD/home>.
- [12] http://physics.bu.edu/NEPPSR/2007/TALKS-2007/NEPPSR_Butler_2007.pdf.
- [13] Wigmans, R., *Calorimetry: Energy Measurements in Particle Physics*. Oxford: Clarendon Press pg. 207 (2000).
- [14] http://physics.bu.edu/NEPPSR/2007/TALKS-2007/NEPPSR_Butler_2007.pdf.

- [15] Thomson, M.A., Particle Flow Calorimetry and the PandoraPFA Algorithm, http://arxiv.org/PS_cache/arxiv/pdf/0907/0907.3577v1.pdf, (2009).
- [16] Boona, S., Scurti, N., Lima, G., Zutshi, V., Hedin, D., (NIU/NICADD) for CALICE Collaboration, Society of Physics Students Congress 2008 (2008).
- [17] <https://twiki.cern.ch/twiki/bin/view/CALICE/CALICEDAQ>.
- [18] The CALICE Collaboration, Preliminary Results from Hadron Shower Data with the CALICE tile AHCAL Prototype, CALICE Analysis Note CAN-003 (2007).
- [19] <http://public.web.cern.ch/public/en/Research/AccelComplex-en.html>.
- [20] The CALICE Collaboration, Study of the Response of the CALICE Silicon-Tungsten Electromagnetic Calorimeter Prototype to Electrons, CALICE Analysis Note CAN-001 (2007).
- [21] The CALICE Collaboration, First Results from Electron Data with the CALICE Tile HCAL Prototype at the CERN Test-Beam, CALICE Analysis Note CAN-002 (2007).
- [22] Garutti, E., AHCAL - practice talk for CALOR'08, <http://nicadd.niu.edu/cdsagenda//askArchive.php?base=agenda&categ=a0813&id=a0813s1t64/transparenties> (2008).
- [23] The CALICE Collaboration, Preliminary Study of the Combined Response of the CALICE Calorimeter Prototypes to Pion Beams, CALICE Analysis Note CAN-004 (2007).
- [24] The CALICE Collaboration, Summary of the 2007 CALICE test beam at CERN (CERN-SPSC-2007-027 SPSC-SR-023) (2007).
- [25] The CALICE Collaboration, CALICE Test Beam E-Log, <https://tftinfo.desy.de/elog/servlet/XMLlist?file=/CALICEelog/data/2007/31/03.08&xsl=/elogbook/xsl/elog.xsl&picture=true#2007-08-03T00:45:20> (2006).
- [26] Summary of the 2007 CALICE Test Beam at CERN (CERN-SPSC-2007-027 SPSC-SR-023) (2007).
- [27] The CALICE Collaboration, Preliminary Study of the Combined Response of the CALICE Calorimeter Prototypes to Pion Beams, CALICE Analysis Note CAN-004 (2007).

- [28] The CALICE Collaboration, Preliminary Study of the Combined Response of the CALICE Calorimeter Prototypes to Pion Beams, CALICE Analysis Note CAN-004 (2007).
- [29] The CALICE Collaboration, Preliminary Results from Hadron Shower Data with the CALICE tile AHCAL Prototype, CALICE Analysis Note CAN-003 (2007).
- [30] CALICE Test Beam E-Log (2006).
- [31] Garutti, E., Private correspondence (2009).
- [32] Danilov, M., ITEP (Moscow) for the CALICE Collaboration, SiPM for CBM, <http://www.gsi.de/documents/DOC-2004-Nov-91-2.pdf> (2004).
- [33] Sefkow, F., DESY, for the CALICE Collaboration, The Scintillator HCAL Testbeam Prototype, http://www.slac.stanford.edu/econf/C050318/talks/0914_TALK.PDF (2005).
- [34] Sefkow, F., DESY, for the CALICE Collaboration, The Scintillator HCAL Testbeam Prototype, http://www.slac.stanford.edu/econf/C050318/talks/0914_TALK.PDF (2005).
- [35] The CALICE Collaboration, Preliminary Results from Hadron Shower Data with the CALICE Tile AHCAL Prototype, CALICE Analysis Note CAN-011 (2008).
- [36] The CALICE Collaboration, Hadronic Shower Response in AHCAL, CALICE Analysis Note CAN-011_update (2008).